Computational study of ionic liquids with metal-based anions for gas separation/absorption

Andreia da Palma Fonseca
Master's Degree in Chemistry
Department of Chemistry and Biochemistry
2022

Supervisor
Iuliia Voroshylova, Researcher, LAVQ@REQUIMTE

Co-supervisor
Natália Cordeiro, Associate Professor, Faculty of Sciences of the University of Porto


U.PORTO
FACULDADE DE CIÊNCIAS
UNIVERSIDADE DO PORTO

Dedicated to AEFCUP and my grandmother

Acknowledgements

To my supervisor, Iuliia Voroshylova, thank you for giving me the opportunity to do an internship in an area that interests me, for the ideas, knowledge, and opportunity to carry out this project. For accompanying me throughout this project, for the willingness you always showed to help in any way necessary and for the little tricks you taught me.

To Prof. Natália Cordeiro for welcoming me into her working group, for welcoming me with open arms and to Elisabete and Nádia for helping me to join this group, thank you for your dedication and teachings.

A big thank you to my friends! Because without you this journey wouldn't have been the same. Thank you for always being there and being a pillar for me. Thank you for trusting me, for the laughs, the dramas, and the good times.

To my figure skating colleagues, thank you for all your help, advice, friendship, good times, your trust in me and for always being in line with my ideas.

Finally, thank you to AEFCUP, who I consider my second family. To all those who accompanied me as I grew up and for all the support and trust they always had in me. For all the years, for all the memories and for never abandoning me. You made me what I am today.

Resumo

Com o aumento dos problemas ambientais, o aumento das emissões de gases com efeito de estufa (como o CO_2 ou o CH_4) e outros gases potencialmente perigosos (como o NH_3 e o SO_2) tornou-se uma das maiores preocupações mundiais, pelo que a sua captura e separação eficaz torna-se necessário. Esta minimização das emissões de gases ajuda a mitigar problemas ambientais, como o aquecimento global. Além disso, alguns dos gases, potencialmente perigosos, podem encontrar aplicações noutros domínios: o CO_2 e o NH_3 podem ser utilizados para a síntese de outros compostos orgânicos, materiais e produtos químicos [1].

Os líquidos iónicos (LI), uma classe de sais orgânicos com baixos pontos de fusão (menos de 100 °C) e baixas pressões de vapor, têm sido estudados para a separação de gases desde o início da década de 2000, embora o primeiro registo sobre os LI remeta para o ano de 1914 [2]. Uma das características atrativas dos LI é a possibilidade de os sintetizar com diferentes combinações de catiões e aniões, controlando assim a sua seletividade e solubilidade em relação a diferentes gases [3]. Os líquidos iónicos magnéticos (MIL) revelaram-se uma escolha comum para a captura de gases, uma vez que respondem a campos magnéticos externos devido aos átomos paramagnéticos incorporados; podem também ser altamente hidrofóbicos e apresentar uma grande suscetibilidade magnética [4]. Os aniões metálicos de cloreto têm geralmente uma excelente capacidade de adsorção de NH_3 ou CO_2, uma vez que estas moléculas contêm pares de eletrões não partilhados e, consequentemente, podem atuar como ligandos.

Neste trabalho, realizámos simulações de MD utilizando o pacote de software GROMACS 2020.4, uma técnica rápida e amiga do ambiente. Concentramo-nos na adsorção de CO_2 em MILs baseadas no catião trihexil(tetradecil)fosfónio, $[P_{66614}]^+$, acoplado a aniões metálicos de cloreto (Fe(III), Mn(II) e Gd(III)). O $[P_{66614}][FeCl_4]$ foi também explorado quanto à possibilidade de captura de outros gases potencialmente perigosos. Os resultados mostram que em $[P_{66614}][FeCl_4]$ apenas a adsorção de SO_2 ocorre espontaneamente, enquanto para todos os outros gases, o ΔG é positivo. Os dois outros MILs apresentam energias de adsorção de CO_2 negativas, o que as torna promissoras candidatas a absorventes de CO_2. Como esperado, em todos os casos favoráveis à absorção de gases, temperaturas mais baixas promovem o processo.

Palavras-chave: líquidos iónicos magnéticos, dinâmica molecular, gases de estufa, captura de CO_2.

Abstract

With the rise of environmental concerns, the increase in emissions of greenhouse gases (such as CO_2 or CH_4) and other potentially dangerous gases (such as NH3 and SO2) has become a major preoccupation, so their effective capture and separation becomes necessary. Minimizing the gases emission helps to mitigate such environmental problems, as global warming. Furthermore, some of the potentially dangerous gases can find their application in other fields: CO_2 and NH_3 can be used for the synthesis of other organic compounds, materials, and chemicals [1].

Ionic liquids (ILs), a class of organic salts with low melting points (less than 100 °C) and low vapor pressures, have been studied for gas separation since the beginning of the 2000s, although the first record on ILs dates to 1914 [2]. One of ILs' attractive feature is the possibility to synthesize them with different combinations of cations and anions, thus controlling their selectivity and solubility towards different gases [3]. Magnetic ionic liquids (MILs) have turned out to be a common choice for gas capture since they respond to external magnetic fields due to incorporated paramagnetic atoms; they can also be highly hydrophobic and present large magnetic susceptibility [4]. Chlorometallate anions generally have excellent NH_3 or CO_2 adsorption capacity, as these molecules contain unshared electron pairs and consequently can act as ligands.

In this work, we performed MD simulations using GROMACS 2020.4 software package, a fast and eco-friendly technique. We focus on the adsorption of CO_2 in MILs based on trihexyl(tetradecyl)phosphonium cation, $[P_{66614}]^+$, coupled with chlorometallate (Fe(III), Mn(II) and Gd(III)) anions. $[P_{66614}][FeCl_4]$ was also explored for the possibility of other potentially dangerous gases capture. The results show that in $[P_{66614}][FeCl_4]$ only the adsorption of SO_2 occurs spontaneously, while for all other gases, the ΔG is positive. Two other MILs present negative CO_2 adsorption energies, making them promising candidates for CO_2 scavengers. As expected, lower temperatures promote the process in all cases favourable for gases absorption.

Keywords: magnetic ionic liquids, molecular dynamics, greenhouses gases, CO_2 capture.

Table of Contents

List of Tables

List of Figures

List of Abbreviations

$[BMIM]^+$	1-butyl-3-methylimidazolium
$[EMIM]^+$	1-ethyl-3- methylimidazolium
$[P_{66614}]^+$	trihexyl(tetradecyl)phosphonium
COM	centre of mass
EMD	equilibrium molecular dynamics
ER	Einstein Relation
FF	force field
GKM	Green-Kubo Method
IL	ionic liquid
MD	molecular dynamics
MIL	magnetic ionic liquid
NEMD	non-equilibrium molecular dynamics
OPLS-AA	optimized potentials for liquid simulations - all atoms
RDF	radial distribution function
SDF	spatial distribution function
VACF	velocity autocorrelation function

1. Introduction

The evolution of technology, the increase in productivity, and the amount of material produced, along with energy expenditure, has led to an increase in greenhouse gases and other that can be prejudicial to the environment. The greenhouse gases absorb the heat radiated by the planet, leading to extreme weather events, thus increasing concerns, and making it urgent to create effective strategies to capture these gases. According to Eurostat data, in 2021, emissions of these gases were 3.6 billion tonnes of CO_2 equivalent in the European Union, essentially carbon dioxide, CO_2 (around 80%), followed by methane, at around 12% [5]. Apart from these environmental issues, these dangerous gases if captured can be reused for other purposes: CO_2 has applications in the synthesis of organic compounds; NH_3 is involved in various processes in the fields of agriculture, and pharmaceuticals, among others; methane can be used to generate energy, as it is the main component of natural gas [6]; SO_2 is often used as a conservative and whitener of food [7].

In the sense of developing processes that allow the separation and capture of these gases, ionic liquids (ILs) have shown to be an interesting choice of study for this purpose, mainly due to their outstanding properties (low vapor pressure and melting point, ease in adjustment of composition to control gas solubility and selectivity) [3].

Currently, a new subclass of ILs - magnetic ionic liquids (MILs) - has been subjected to scrutiny, since they are highly hydrophobic and present large magnetic susceptibility, which makes them promising solvents for separations. MILs, due to the incorporated paramagnetic component - a metal ion – respond to an external magnetic field [8], [9]. In addition, the choice of metal chloride anions could make these MILs even more promising, as they generally have excellent adsorption capacity for NH_3 or CO_2, since these molecules contain unshared electron pairs and can act as ligands [10].

Minding modern environmental challenges, molecular dynamics (MD) simulations become a desirable investigation method, allowing avoiding waste of reactants and at the same time obtaining insights on the studied systems. This method, which numerically solves Newton's equations of motion for the system of many interacting particles (atoms or molecules, for example, described by pair effective potentials), allows us to have a prediction of the properties of MILs, as well as their potential for greenhouse gas capture. However, the efficiency of MD simulations is limited by the

quality of the employed force fields (FFs), which performance must be validated. Thus, we tested several validation methods [11] on the example of MILs based on triphenyl(tetradecyl)phosphonium cation, $[P_{66614}]^+$, coupled with metal (Fe, Gd, Mn) chloride anion. The choice of these anions, with different numbers of pairs of unshared electrons, 1, 2 and 3 pairs respectively, allowed us to see how these unpaired electrons can be beneficial in capturing gases, as it has already been seen in other studies with different ILs [10],[12]. Namely, transport properties of the simulated systems using FFs previously developed in our group were tested by different methods: non-equilibrium MD, Green-Kubo, and Einstein relation for viscosity and mean square displacement and velocity autocorrelation functions for self-diffusion. To complete the investigation, the density, and enthalpy of vaporisation were computed. Structural features analysis in terms of radial and spatial distribution functions was also carried out.

In this context, the final objective of this work was to describe the adsorption of the greenhouse pollutant gas, CO_2, by these MILs. The $[P_{66614}][FeCl_4]$ was also tested for the possibility of capturing other potential gases, namely sulphur dioxide, SO_2, ammonia, NH_3, and methane, CH_4. The solvation free energy was calculated, as well as the structural features were analysed in the systems studied. The effect of temperature was also addressed.

1.1. Ionic Liquids (ILs)

Ionic liquids represent a class of organic salts that have garnered significant attention due to their low melting points, typically below 100°C. They are seen as promising alternatives to volatile organic solvents. The inception of ionic liquids dates back to 1914 when the first synthesis of such a compound was documented. Specifically, ethylammonium nitrate, $[EtNH_3]$ $[NO_3]$, was successfully synthesised through the concentrated addition of nitric acid with ethylamine [13].

ILs are composed of either organic or inorganic anions combined with organic cations, such as N´-substituted imidazolium, tetra-alkylated ammonium, tetra-alkylated phosphonium, among others [2]. Brennecke and Maginn, in their work, [14] reported the difficulty of packing the ILs' ions, due to the fact that they often feature large cations paired with small anions. Such disparity in sizes is the primary reason behind the inability of ILs to crystallize, allowing them to remain in a liquid state at room temperature. Besides, the vast array of possible combinations of cations and anions

enables the tailoring of ILs properties, such as selectivity and solubility towards different gases.

Furthermore, ionic liquids exhibit low vapour pressure or non-volatility under ambient conditions, making them a green substitute to volatile organic solvents like acetone, since they do not affect atmospheric photochemistry [15]. Due to such properties, ILs have been the target of study towards more efficient and more environmentally friendly processes. However, care must be taken in the process of synthesis of these compounds on a large industrial scale, since in some cases, the production of ILs can generate a large amount of waste of chemicals and reagents, potentially having negative environmental impacts. Consequently, the synthesis methods of ILs do not always satisfy the principles of green chemistry [2].

Other properties are important for the final application of ionic liquids too. When it comes to density, one can see that the values generally vary between 1.0 g cm^{-3} and 1.6 g cm^{-3}, so they are denser than water and organic solvents [16]. Some experimental data show a decrease in density as temperature rises and also when the length of an alkyl chain in either the cation or anion of imidazolium-based ILs increases [17]. The alkyl chain size can also lower or increase the melting point and/or other properties, which are important features for industrial applications.

The high viscosity of ionic liquids is a drawback that limits their efficiency in numerous electrochemical devices[18]. Typically, the viscosity of ionic liquids is greatly affected by the presence of impurities, even in small quantities, such as the presence of water [18]. However, understanding the influence of the structural components makes it possible to overcome some of these problems.

ILs have found applications in different processes, such as in separation and extractions, electrochemistry, solvents, and catalysts, etc [2].

1.1.1. Magnetic Ionic Liquids (MILs)

A new subclass of ILs, magnetic ionic liquids (MILs), has recently appeared and sparked keen interest among many scientific groups [9],[19],[20]. These solvents respond to an external magnetic field, once they incorporate in their structure a paramagnetic component, a metal ion [9]. The first MIL reported in the literature was [Bmim][$FeCl_4$], 1-butyl-3-methylimidazolium tetrachloroferrate, which was already a known IL. However, its magnetic properties have been demonstrated in 2004 by Hayashi and

Hamaguchi, using superconducting quantum interference device (SQUID) magnetometry [21].

With the discovery of magnetic properties of ILs, the research on this area has increased, and a variety of MILs based on others transition metals, for example, manganese, cobalt, and gadolinium[22] were produced and analysed. Due to its comparatively low cost and greater availability compared to others MILs, 1-ethyl-3-methylimidazolium, $[Emim]^+$, and 1-butyl-3-methylimidazolium, $[Bmim]^+$, and $[P_{66614}]^+$ are the most used cations in the synthesis of magnetic ionic liquids.

Recently, gadolinium, neodymium and dysprosium, rare earth metals [23],[24], were incorporated into magnetic ionic liquids, showing a strong response to magnetic field, and, sometimes, luminescence properties. Albo et al. [25] and Sesto et al. [22] reported similar procedures to synthesise MILs. The synthesis consists of adding iron (III) chloride hexahydrate, manganese chloride, or gadolinium (III) chloride hexahydrate to a solution of $[P_{66614}][Cl]$ in dichloromethane. After the solution is stirred at room temperature, the organic phase is dried over magnesium sulphate and the solvent is removed under vacuum.

Like in the case of conventional ILs, it is possible to design the physicochemical properties of MILs for specific applications, by modifying the cation or anion. When compared with ferrofluids, MILs are transparent and exist as neat magnetic solvents [22], unlike the usual solvents which require suspended magnetic particles to convey magnetic properties to the bulk material. Furthermore, magnetic ionic liquids do not need dispersants or stabilising organic solvents because they exhibit low volatility [19]. However, some MILs, in aquatic ecosystems, may pose risks, because some of them are soluble in water [9]. MILs have many applications in chemical processes, such as fluid-fluid separation, as well as in electrochemical and medical devices [9].

1.1.2. Properties of Magnetic Ionic Liquids

The choice of the cation and the anion has a large impact on the final MIL characteristics. The increase in the alkyl chain of the components leads to an increase in the interionic van der Walls interactions and, consequently, a change in the ions diffusion [26]. This is only an example, so it is important to understand the relationship between the differences in structures and the various properties.

Indeed, many of the applications of MILs in analytical chemistry are influenced by their viscosity, considering that specific values are desirable for different methods and procedures. For example, MILs with lower viscosities help mass transfer in extraction procedures, whereas in techniques such as gas chromatography (on the stationary phase) more viscous MILs are preferred [19].

Generally, the Orrick – Erbar model [27] is used to estimate the temperature-dependent effects on viscosity, expressed as follows:

$$ln\left(\frac{\mu}{\rho M}\right) = A + \frac{B}{T} \quad (1)$$

where μ is viscosity (cP), ρ is density (g cm^{-3}), M is molecular weight (g mol^{-1}), T is the absolute temperature (in K), and A and B are the Orrick–Erbar parameters. According to Robert et al. [27], one should use the density value at 293 K for liquids with boiling point below 293 K.

Daniel et al. [28] decided to apply this model in some MILs with the phosphonium cation $[P_{66614}]^+$, and the values obtained show a good agreement with the experimental values. In this study, they also showed, for example, that the phosphonium cation has a lower impact compared to imidazolium, pyridinium, and pyrrolidinium cations and that the influence of the anion on viscosity across temperatures is more significant. Another study [4] with the cation $[P_{66614}]^+$, demonstrated that MILs with doubly and triply charged anions present a sharp decrease in viscosity when compared with singly charged anions, like $[FeCl_4]^-$.

Similarly, to conventional ILs, the density of MILs decreases with increasing temperature. A study [4] on $[P_{66614}]_2[MnCl_4]$ MILs yielded the expected results, namely: At 293.15 K, the density of the MIL equals to 0.965 g cm^{-3} while when the temperature increases to 303.15 K, the density decreases to 0.959 g cm^{-3}. The hydrophobicity of MILs also has an impact on their final application. Indeed, hydrophilic MILs can be used to store electrolytes in batteries.

1.2. Molecular Dynamics

Molecular dynamics (MD) is a computer simulation technique, which was introduced by Alder and Wainwright in the late 1950s, to study the behaviour of rigid spheres undergoing perfect elastic collisions [29]. This technique is based on the numerical

integration of Newton's equations of motion for an interacting system of atoms or molecules over time [30]. It enables us to predict molecular structures, thermodynamic properties, and dynamics in an eco-friendly manner, avoiding the wastage of reactants.

The efficiency of MD simulations is inherently tied to the quality of the employed force fields (FFs). These FFs contemplate molecular features to reproduce selected properties of the system, like the time evolution of bond lengths, non-bonding van der Waals interactions, and inter-atomic interactions, among others [31].

Once the forces or intermolecular potential energy are known, classical Newton's laws of motion are applied to calculate positions at successive times, and consequently the micro-states of the system over time by updating the positions of the atoms, resulting in a set of coordinates that form the trajectory [31].

From Newton's second law of motion, we know that the force, *F*, is equal to the product of the particle's *i* mass, m_i, and acceleration, a_i:

$$F_i = m_i a_i \tag{2}$$

Along with that, a_i is the second order derivative of position, r_i, with respect to time, *t*:

$$a_i = \frac{d^2 r_i}{dt^2} \tag{3}$$

Considering equations (2) and (3), we get the equations of motion used to obtain the trajectory of each particle within the simulated system:

$$\frac{d^2 r_i}{dt^2} = \frac{F_i}{m_i} \tag{4}$$

However, these equations are impossible to solve analytically for systems with more than two atoms. Because of this, it is necessary to solve them numerically, using one of several integration algorithms, to obtain the values of velocities and positions of the particles at successive times. Equations (5) and (6) show the Leapfrog method for integration. First, the velocities in time $\left(t + \frac{1}{2}\delta t\right)$ are calculated, and then, using the value of velocity obtained, it is possible to calculate the positions at time $(t + \delta t)$:

$$v\left(t+\frac{1}{2}\delta t\right) = v\left(t-\frac{1}{2}\delta t\right) + a(t)\delta t \quad (5)$$

$$r(t+\delta t) = r(t) + v\left(t+\frac{1}{2}\delta t\right)\delta t \quad (6)$$

As such, the obtained trajectory is not continuous, but discrete, with the points separated by a constant time interval δt – the MD time step, which should be shorter than the time of molecular relaxations. The various properties of the system can then be calculated by averaging the results gathered along this discrete trajectory [32].

It should be noted that not all force fields are universally applicable to all types of molecules. However, as research advances, efforts have led to the development of equivalent force fields tailored to specific needs.

In this particular study, the Optimized Potential for Liquid Simulations (OPLS) all-atom (AA) force field [33] was employed, with several refinements developed in the group. The OPLS-AA force field is known for its efficiency and versatility in describing various molecular parameters across a wide range of molecular structures. Its successful application in this study underscores its suitability for simulating the systems under investigation.

2. Systems and Methods

2.1. Systems

In this work, the MILs under investigation consist of phosphonium cations and metal chloride anions, both of which contain unshared electron pairs and can thus act as ligands. Furthermore, the chosen systems have already been studied [4] and have shown promise in the capture of gases such as CO_2. Namely, the selected systems include:

- Phosphonium tretrachloroferrate: $[P_{66614}][FeCl_4]$
- Phosphonium tretrachloromanganese: $[P_{66614}]_2[MnCl_4]$
- Phosphonium hexachlorogadolinium: $[P_{66614}]_3[GdCl_6]$

Figure 1 shows the optimised geometries of the studied cation and anions.

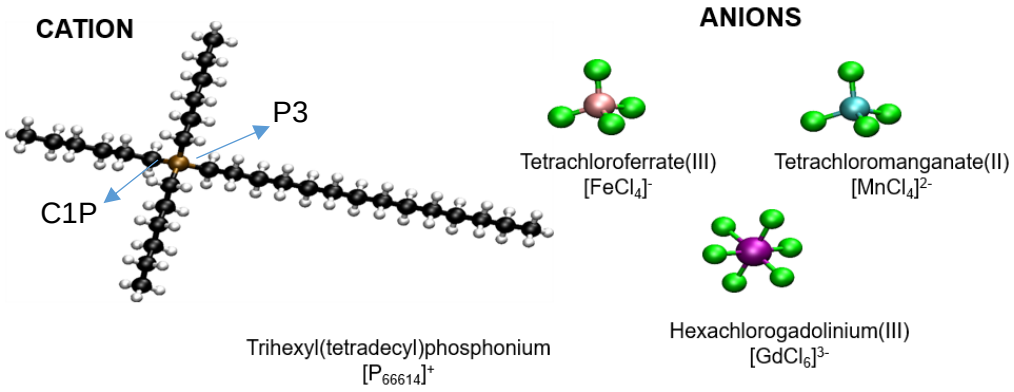

Figure 1. Optimised geometries of the studied ions. The black, white, brown, green, pink, cyan, and purple spheres represent carbon, hydrogen, phosphorus, chlorine, iron, manganese, and gadolinium atoms, respectively.

Table 1 provides details regarding the composition of the MD simulated systems, including the number of interacting sites and the resulting size of the simulation box.

Table 1. Composition of the simulated systems and details about the simulation box used.

MIL	Number of cations	Number of anions	Total number of atoms	Cubic box size/nm^3
$[P_{66614}][FeCl_4]$	219	219	23214	7.0 × 7.0 × 7.0
$[P_{66614}]_2[MnCl_4]$	220	110	22770	7.0 × 7.0 × 7.0
$[P_{66614}]_3[GdCl_6]$	219	73	22630	7.1 × 7.1 × 7.1

The MD simulations in this work focused on the following gases: carbon dioxide, CO_2, sulphur dioxide, SO_2, ammonia, NH_3, and methane, CH_4. Figure 2 displays all – atom (AA) geometries of CO_2, SO_2, NH_3 and united atom (UA) geometry of CH_4.

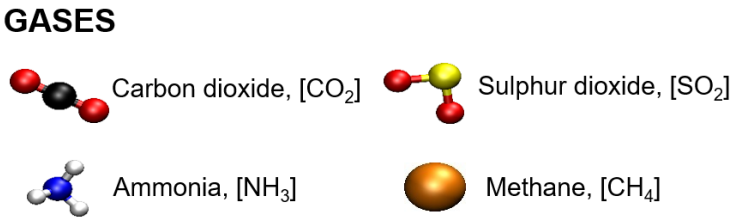

Figure 2. Optimised geometries for CO_2, SO_2, NH_3 and geometry of CH_4 model gases. The black, white, red, yellow, and blue spheres represent carbon, hydrogen, oxygen, sulphur, and nitrogen atoms, respectively.

2.2. Computational Setup

All simulations were performed using the software package GROMACS 2020.4. The systems with the constitution mentioned in table 1 were randomly placed in a cubic box, with the help of the Packmol program.

First, the steepest descent method was applied for energy minimisation, followed by a system relaxation run, in the canonical ensemble (NVT) for a short period (1 ns). This was followed by the equilibrium run, in the isothermal-isobaric ensemble (NpT) for 30 ns. The Berendsen barostat and v-rescale thermostat were employed to maintain the pressure at 1 bar and temperature at 298.15 K. The density was assessed from the last 10 ns of the equilibrium run with Gromacs in-built tools.

Then, several production runs were performed for each system, according to the properties to study and analyse. For dynamic properties, sampling an NPT run for 25 ns with a 0.002 ps time step was performed. The mean square displacement, MSD, for further self-diffusion assessment and stress tensor components for further viscosity assessment were collected. During the production run, the Nosé-Hoover thermostat with a coupling constant of 0.8 ps, and the Parrinello-Rahman barostat with a coupling constant of 2.0 ps, were used. To perform non-equilibrium MD simulations of viscosity, the run was shorter (15 ns), with an acceleration of 0.01 nm ps^{-2}. A v-rescale thermostat with a coupling constant of 0.5 ps was utilised. To obtain the trajectory for the calculation of structural properties, a separated production run of 1 ns in the NVT ensemble with a Nose-Hoover thermostat was carried out.

The performance of general FF can be improved with the adjustment of partial charges. Therefore, for the cation, the set of partial charges taken from the OPLS-AA force field

reported by Canongia Lopes and Pádua [34] was used, while for anions the partial charges used were previously developed in our group.

The calculation of the free energy of solvation was based on the BAR (Bennett acceptance ratio) method, which is based on the calculation of a ratio of the weighted average of the Hamiltonian difference of state B in relation to state A and vice versa. So to calculate the free energy of solvation, we first equilibrated the previous systems with one molecule of each gas. The same protocol was used, from the creation of the box, through the minimisation of energy, plus NVT, and NpT equilibration runs, under the conditions previously explained. After that, a script was applied (see Annex 1), having different parameter files based on the definitions used by Shirts et al [35]. When creating the file with the topology information, the charges were set to zero, otherwise, it could result in a very unstable system, with the approach of the positive and negative charges, and moreover, our goal is only to transform the van der Walls interactions. After that, considering the already tested procedure, the number of λ values were defined (λ is a coupling parameter indicating the level of change between the two states to be considered). The initial λ value equals to 0.0 for van der Waals, representing state 1, λ = 0.05 represents state 2, and so on, until state 21, representing the end state with λ = 1.0. For each value of lambda, which will be discussed later, it is necessary to run four simulations: steepest descent energy minimisation; NVT equilibration; NpT equilibration; and data collection at the NpT ensemble.

Initially, an energy minimisation run was performed, followed by a NVT run for 100 ps. The Langevin integrator was used to avoid excessive damping of the fluid dynamics. In the NpT equilibration, the Parrinello-Rahman barostat was used to maintain the pressure at 1 bar. The thermostat is implicitly handled by the integrator. In the production MD run, the same barostat and thermostat were applied, with a coupling constant of 1.0 ps. Only when all simulations of all λ values are finished (i.e., when the script runs to the end) can the data be collected and analysed.

2.3. Properties calculations

2.3.1. Density

Density is one of the most relevant physical properties and is defined as the mass of the substance per unit volume, as described in the following equation:

$$\rho = \frac{m}{V} \tag{7}$$

In this case, the densities were calculated using GROMACS in-built tools after the equilibration run, considering equation 7.

2.3.2. Viscosity

The shear viscosity is one of the most critical properties to describe MILs. There are essentially two approaches for calculating properties like viscosity:

1. **Equilibrium Molecular Dynamics** (EMD): In this approach, properties are calculated using temporal correlation function theories within equilibrium simulations. The Green-Kubo Method and the Einstein Relation are two commonly employed techniques within this framework.
2. **Non-Equilibrium Molecular Dynamics** (NEMD): In contrast, NEMD simulations involve imposing a gradient or perturbation in the system and observing how it responds to calculate transport properties directly.

2.3.2.1. Non-Equilibrium

This approach is based on the response of the system – the measured momentum flux, for example, when subjected to an external perturbation [36]. The removal of the generated heat is done by coupling it to a heat bath. Adding force to the liquid results in the generation of a velocity gradient. The applied force must be chosen so that there is no pressure gradient in the x direction, so the acceleration components a_y and a_z must be equal to zero, and a_x is just a function of the z coordinate. Thus, the equation for the velocity in the x direction of the steady state solution is given by equation (8), since v_y and v_z are equal to zero [37]:

$$a_x(z) + \frac{\eta}{\rho}\frac{\partial^2 v_x(z)}{\partial z^2} = 0 \tag{8}$$

where, $a_x(z)$ is the acceleration, η the viscosity, and ρ the density.

This acceleration is applied in the x direction, which is a function of the z coordinate:

$$a_x(z) = A\cos\left(\frac{2\pi z}{l_z}\right) \tag{9}$$

where l_z is the height of the box.

After that, it is possible to generate the velocity:

$$v_x(z) = V\,cos\left(\frac{2\pi z}{l_z}\right) \tag{10}$$

with the volume *V* given in terms of an arbitrary amplitude parameter *A* by:

$$V = A\,\frac{\rho}{\eta}\left(\frac{l_z}{2\pi}\right)^2 \tag{11}$$

From *A* and *V*, the viscosity can be calculated as follows:

$$\eta = \rho\,\frac{A}{V}\left(\frac{l_z}{2\pi}\right)^2 \tag{12}$$

It is possible to measure the average v, after the amplitude of the velocity profile is fully developed. Furthermore, the velocity profile must be excluded from the kinetic energy to get the correct viscosity value [37].

2.3.2.2. Green Kubo Method

Following the Green-Kubo Method (GKM), the shear viscosity can be calculated by the integral of the autocorrelation function of the pressure tensor over time [38]:

$$\eta = \frac{V}{k_B T}\int_0^\infty \langle P_{\alpha\beta}(t)P_{\alpha\beta}(0)\rangle\,dt \tag{13}$$

The elements of the pressure tensor are calculated by the equation:

$$P_{\alpha\beta}(t) = \frac{1}{V}\sum_j\left[m_i v_{\alpha i}v_{\beta i} + \frac{1}{2}\sum_{i\neq j} r_{\alpha ij}\,f_{\beta ij}\right] \tag{14}$$

where m_i is the mass of particle i, $v_{\alpha i}$ is the velocity, $r_{\alpha ij}$ is the α-component of the vector separating particles i and j, and $f_{\beta ij}$ is the β-Cartesian component of the force between these particles. To improve the viscosity calculations, one often averages the three independent terms of the pressure tensor, P_{xy}, P_{yz}, P_{xz}, since it is not possible to average the number of particles in the system, because shear viscosity is a collective property.

To obtain good results with this method, it is necessary to ensure that the integrand has decayed sufficiently to allow the upper bound on the integral to be truncated. Because of that, when applied to ionic liquids, the autocorrelation calculation of the pressure tensor converges very slowly, implying a very long simulation time, as well

as the tensor components must be stored several times in small time intervals, in order to guarantee the precision of the result [38],[39].

Furthermore, it is crucial to indicate which procedure is used to ultimately calculate the viscosity from equation (13). There are three procedures, namely [11]: averaging over a time interval for which the straight line is more linear, fitting the autocorrelation function to a model and analytically integrating it, or fitting the "running integral" to a model and extrapolating it. In this work, we apply the first procedure presented.

2.3.2.3. Einstein Relation

Instead, the value of the viscosity can be estimated by the Einstein relation (ER) [40]:

$$\eta = \frac{1}{2}\frac{V}{k_B T} \lim_{t \to \infty} \frac{d}{dt} \langle \left(\int_{t_0}^{t_0+t} dt' P_{\alpha\beta}(t') \right)^2 \rangle_{t_0} \quad (15)$$

In this case, there is a relationship of the viscosity with the slope of the generalised root mean square displacement function in the time limit $t \longrightarrow \infty$.

After a few picoseconds, the integral becomes practically linear in a single simulation. As a result, when calculating viscosity, it is advisable to utilise the slope from just one simulation during an intermediate time interval [11].

2.3.3. Self-Diffusion

For the calculation of self-diffusion, a very important transport property to characterise the motion of a single particle, two methods were used, which are equivalent but subject to different errors during the MD simulations.

This property was calculated through the slope of the mean square displacement, using the Einstein Relation, and, alternatively, using the Green-Kubo formulas, it was obtained from the integrals of the time correlation functions.

2.3.3.1. Mean Square Displacement

The mean square displacement (MSD) is a valuable measure in molecular dynamics simulations, representing the average of the squares of displacements from a reference position for each particle over time. Mathematically, it is expressed by equation (16):

$$\mathbf{MSD} = \langle |\boldsymbol{r_i}(\boldsymbol{t}) - \boldsymbol{r_i}(\mathbf{0})|^2 \rangle \quad (16)$$

where r_i is the position of the centre of the mass of the particle at time *t*.

The self-diffusion coefficient was obtained by means of the Einstein relationship:

$$D = \frac{1}{6} \lim_{t \to \infty} \frac{d}{dt} \text{MSD} \quad (17)$$

However, it is necessary to pay attention because the relationship between MSD and time is not always linear (i.e., not always in diffusion regime), and there are zones of anomalous diffusion, due to several factors, such as heterogeneity, complexity of the medium, structure, etc [41]. To determine the location of the different regions of diffusion, the β parameter was calculated [42], according to the following equation:

$$\beta(t) = \frac{d\ log(\Delta r^2)}{d\ log(t)} \quad (18)$$

where Δr^2 refers to the average mean square displacement. Figure 3 shows the relationship between different values of β and its diffusion condition [41]:

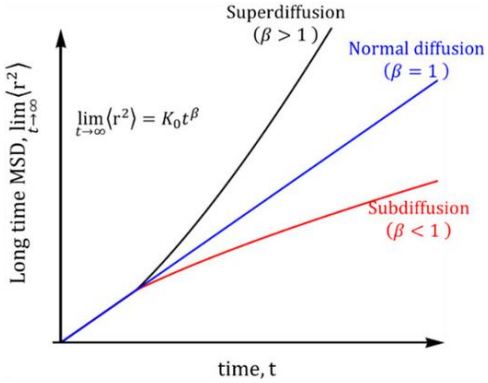

Figure 3. Relationship of mean square displacement with time for different diffusion conditions.

In this work, the self-diffusion coefficients were calculated in the diffusive regime, i.e., for parts of trajectory where β = 1.

2.3.3.2. Velocity Autocorrelation Function

The velocity autocorrelation function (VACF) plays a crucial role for quantifying transport coefficients in dynamic processes, such as the calculation of self-diffusion coefficients under equilibrium conditions.

The application of VACF involves tracking the velocities of particles not only at the current moment but also in previous time steps. Its accuracy is improved by calculating the average for all particles in our system using the following formula [39]:

$$C_v(t) = \frac{\langle v_i^c(t) \cdot v_i^c(0) \rangle}{\langle v_i^c(0) \cdot v_i^c(0) \rangle} \quad (19)$$

where $v^c(t)$ is the velocity of the centre of mass of the ion and the angular brackets represent an ensemble average over all time origins.

The self-diffusion can then be calculated using the Green-Kubo relation, from integrals of the flow-time correlation functions:

$$D_i = \frac{1}{3} \int_0^\infty \langle v_i^c(t) \cdot v_i^c(0) \rangle \, dt \quad (20)$$

2.3.4. Enthalpy of Vaporisation

This property indicates the amount of energy required for a certain quantity of liquid to change into a gaseous substance [38]. The enthalpy of vaporisation (ΔH_{vap}) was obtained from the molar internal energy in the gas and in the liquid phases, at *T* = 298.15 K, following the equation [38]:

$$\Delta H_{vap} = E_{pot}(gas) - E_{pot}(liquid) + RT \quad (21)$$

where *R* represents the universal gas constant.

2.3.5. Structural Analysis

2.3.5.1. Radial Distribution Function

The radial distribution function (RDF) quantifies the probability of finding a particle (i.e.: atoms, molecules) at a distance *r* from a given reference particle in a system of interacting particles. The RDF, denoted as *g*(*r*), is defined as the ratio of the average local particle density at distance *r* to the apparent density of the particles. However, to normalize the histogram for a three-dimensional system, the density is multiplied by the volume of the spherical shell, so the general expression to calculate the RDF is [43]:

$$g(r) = 4\pi r^2(\rho(r) - \rho(0)) \quad (22)$$

where $\rho(r)$ is the density of the particles at distance *r*, and $\rho(0)$ is the bulk density of the particles.

In a system, when *g*(*r*) reaches its first peak, it signifies the distance to the first sphere of particles surrounding the reference particle. This first sphere is often referred to as

the first solvation layer [44]. In liquids, while multiple coordination spheres are possible, the probability of finding particles beyond the first sphere is significantly reduced due to the repulsion exerted by the first sphere, thus, subsequent peaks in the RDF will be much smaller compared to the first peak.

One of the significant advantages of RDFs is the fact that besides being possible to calculate through simulations, it can also be obtained from neutron and X-ray diffraction experiments. This makes the RDF a valuable property for validating simulation results, taking into account that it is possible to compare simulated values with experimental values [45].

2.3.5.2. Spatial Distribution Function

To have a more complete structural picture, the Spatial Distribution Function (SDF) was accessed. SDF represents the three-dimensional distribution of spatial density in a coordinate system defined by a central molecule, covering both radial and angular coordinates [46],[47].

Since this is a probability distribution in three-dimensional space, its function is inherently four-dimensional, so it is necessary to reduce it to make it easier to visualise. To do so, iso-surfaces are employed, which are surfaces that pass with the same probability through all areas. The iso-surface values, habitually expressed in units like nm^{-3} or pm^{-3}, specify the density of the particles along the iso-surface. In conclusion, the SDF is an iso-surface of the density of particles around a fixed molecule [45].

2.3.6. Free energy of solvation

The free energy of solvation is a fundamental physical quantity that characterises the transformation of a system from one state (state A) to another state (state B). This transformation can be described by a coupling parameter λ, which indicates the extent of the change or perturbation in the system's Hamiltonian as it transitions from one state to another [48].

To describe the dynamics of the systems and account for such transformation, an extended Hamiltonian is used. This extended Hamiltonian is defined as follows:

$$H_{extended}(X,\{\lambda\},\{x\}) = T_x + T_\lambda + V(X,\{\lambda\},\{x\}) + V_{bias}(\{\lambda\}) \quad (23)$$

where, T_x and T_λ stand for the kinetic energies of the atomic coordinates and λ variables, respectively, $V(X,\{\lambda\},\{x\})$ is the hybrid potential energy, and V_{bias} is a biasing potential used to facilitate transitions among the substituents at each site [48].

In MD simulations using this extended Hamiltonian, λ is treated as a dynamic variable, allowing for the sampling of intermediate conditions during a single simulation. By running simulations with different values of λ, a curve can be generated. From this curve, the free energy of solvation (ΔG) can be derived [48]. The value of ΔG represents the energetic cost or gain associated with the transformation from state A to state B.

Typically, λ-spacing values of 0.05-0.1 are employed for decoupling Coulombic interactions. These values depend linearly on λ. Equidistant λ spacing from 0 to 1 is usually sufficient for these interactions. However, for the decoupling of van der Waals interactions, more points may be needed to correctly describe the transformation. In such cases, the steepest area of the curve is used and λ points are often grouped together [49],[50].

For each value of λ, the simulation typically involves several steps, including energy minimisation, equilibrium simulations (NVT and NpT ensembles), and then production runs for data collection. These steps are necessary to accurately sample the configuration space and compute the free energy change associated with the solvation process.

3. Results

3.1. Validation

The force field to be used in this study was previously developed in our research group. Thus, the first stage of this work involved judging whether it could produce reliable and accurate data. For validation, we choose a set of dynamical and thermodynamic properties, as discussed in the previous section, and these were estimated through different computational methods using the FF. Afterwards, the simulated results obtained for such properties were analysed and compared with experimental data from the literature.

3.1.1. Density

The simulated density values are compared with the available experimental data in Table 2:

Table 2. Experimental and simulated densities for the studied MILs at *T* = 298.15 K with the respective errors.

MIL	ρ_{sim} /g cm^{-3}	SD_{sim} [a]	ρ_{exp} /g cm^{-3}	error/%
$[P_{66614}][FeCl_4]$	1.005	0.001	1.008	0.30
$[P_{66614}]_2[MnCl_4]$	0.939	0.001	0.949	1.05
$[P_{66614}]_3[GdCl_6]$	0.978	0.003	0.981	0.27

[a] SD refers to the standard deviation of the simulated values.

These and the following reference to errors stand for:

$$error\ (\%) = \frac{|x_{sim} - x_{exp}|}{x_{exp}} * 100 \quad (24)$$

where x_{sim} and x_{exp} indicate the simulated and experimental values for property x.

As can be seen, the predicted density (ρ) values for the three systems show good agreement with experimental data and have low relative errors.

3.1.2. Viscosity

To determine the most suitable approach for calculating viscosity in the studied systems, we employed three distinct techniques. It is worth noting that, for systems

with higher viscosities, the NEMD approach is recommended due to the extreme difficulty of obtaining accurate results using the EMD approach.

Furthermore, in order to fully assess viscosity performance, these calculations were carried out at two different temperatures, namely: 298.15 K and 373.15 K. This choice was made because the dynamics of viscous systems can exhibit significant temperature-dependent variations.

Table 3. Experimental and simulated viscosity for the studied MILs at 298.15 and 373.15 K (estimated with different methods) with the respective errors.

Method	MIL	Temperature/K	η_{sim} /mPa s^{-1}	SD_{sim}	η_{exp} /mPa s^{-1}	error/%
Non - Equilibrium	$[P_{66614}][FeCl_4]$	298.15	699	254	650	7.56
		373.15	77	4	44	75.84
	$[P_{66614}]_2[MnCl_4]$	298.15	719	279	75230	99.04
		373.15	748	319	920	18.72
	$[P_{66614}]_3[GdCl_6]$	298.15	799	345	18390	95.65
		373.15	279	109	290	3.79
Green Kubo Method	$[P_{66614}][FeCl_4]$	298.15	461	12	650	29.1
		373.15	61	29	44	38.64
	$[P_{66614}]_2[MnCl_4]$	298.15	2649	945	75230	96.48
		373.15	1773	755	920	92.71
	$[P_{66614}]_3[GdCl_6]$	298.15	5984	408	18390	67.46
		373.15	890	428	290	206.9
Einstein Relation	$[P_{66614}][FeCl_4]$	298.15	409.5	0.2	650	37.01
		373.15	52.08	0.05	44	18.36
	$[P_{66614}]_2[MnCl_4]$	298.15	2441.2	0.3	75230	96.76
		373.15	1162.4	0.4	920	26.35
	$[P_{66614}]_3[GdCl_6]$	298.15	3477.5	0.6	18390	81.09
		373.15	570.2	0.7	290	96.62

When applying the NEMD approach, one can observe that for the IL $[P_{66614}][FeCl_4]$, it yielded viscosities closer to experimental values, particularly at lower temperatures. However, with increasing temperature, this method did not show the expected effectiveness. The other systems show a quite high viscosity at 298.15 K, which, however, decreases notably with the increase of temperature. This reduction in viscosity was accompanied by a significant decrease in error, resulting in a closer alignment with experimental values.

The Green-Kubo method did not prove to be effective under any of the conditions. This can be attributed to the generally inadequate statistics obtained for highly viscous liquids using this method within the accessible simulation time scales. Indeed, the autocorrelation calculation of the pressure tensor, a requirement for the Green-Kubo method, exhibits slow convergence. Furthermore, this method is considered somewhat arbitrary. Hess [37] also pointed out that this method is not as appropriate as the Einstein Relation for viscosity calculations. They demonstrated that inaccuracies in correlations within the Einstein Relation can be mitigated by focusing solely on short-term integrals.

Upon analysing the values obtained with the Einstein Relation, we observed a general trend where increasing temperature (resulting in less viscous MILs) brought the values closer to experimental ones. For instance, in the $[P_{66614}]_2[MnCl_4]$ system, it was possible to reduce the error from 96.76% to 26.35% by increasing the temperature.

3.1.3. Self-Diffusion

As previously stated, two different methods were employed to investigate this property, with the aim of determining which one is the most appropriate for studying the selected systems. The results obtained are shown in Table 4:

Table 4. Simulated self-diffusion values at 298.15 K and 373.15 K, with respective standard deviations.

Method	MIL	Temperature /K	D_{an} x 10^{-11} /m^2 s^{-1}	SD_{sim}	D_{cat} x 10^{-11} /m^2 s^{-1}	SD_{sim}
Mean Square Displacement	$[P_{66614}][FeCl_4]$	298.15	0.15	0.06	0.079	0.007
		373.15	0.20	0.02	0.12	0.03
	$[P_{66614}]_2[MnCl_4]$	298.15	0.014	0.008	0.071	0.009
		373.15	0.031	0.007	0.052	0.005
	$[P_{66614}]_3[GdCl_6]$	298.15	0.043	0.008	0.063	0.006
		373.15	0.056	0.005	0.021	0.001
Velocity Autocorrelation Function	$[P_{66614}][FeCl_4]$	298.15	13.03	0.01	11.000	0.006
	$[P_{66614}]_2[MnCl_4]$		8.00	0.01	9.330	0.005
	$[P_{66614}]_3[GdCl_6]$		6.033	0.008	8.670	0.006

Unfortunately, no experimental data for these MILs diffusion were found. However, considering the values of these properties for similar ILs, our values are in the expected

range [51],[52], especially the method based on the MSD, where the values range from 10^{-12} to 10^{-11}.

Both methods revealed that two possible trends might exist: the diffusion values of each ionic species, whether cation or anion, can be higher. This suggests a complex interplay of different factors within the systems. On one hand, the anion is significantly smaller, making its movement simpler, while the long alkyl chains of the cation complicate its diffusion. On the other hand, the anion, with its stronger charge concentration, exhibits greater interactivity, which slows it down. Accordingly, in approximately half of the situations (as shown in Table 4), a higher diffusion coefficient is registered for either ion. Two noteworthy observations emerge: (i) both methods consistently indicate higher diffusion for the same ion at the same temperature, and (ii) for $[P_{66614}]_3[GdCl_6]$, a reversal of diffusion values occurs. While at 298.15 K D_{cat} is higher, at 373.15 K, D_{an} rises and surpasses the D_{cat} value. This indicates a stronger interaction of the cation (and weaker interaction of the anion) within this MIL at higher temperatures.

The overall impact of temperature on diffusion can be exemplified by the obtained MSD values. As expected, an increase in the diffusion coefficients with increase of temperature is observed.

3.1.4. Enthalpy of Vaporisation

The results for the enthalpy of vaporisation were obtained by applying equation (21) and are provided in Table 5 below.

Table 5. Simulated enthalpies of vaporisation at 298.15 K, with respective standard deviations.

MIL	ΔH_{vap} x 10^2 /kJ mol^{-1}	SD_{sim}
$[P_{66614}][FeCl_4]$	3	7
$[P_{66614}]_2[MnCl_4]$	4	7
$[P_{66614}]_3[GdCl_6]$	6	11

No experimental values for ΔH_{vap} were found in literature. Nevertheless, our obtained values align with the findings reported in Ref. [53], where the cumulative effect of hydrocarbon chains on the cation led to an increase in ΔH_{vap}.

Furthermore, it was demonstrated that this property increases with the size of the anion. Thus, taking the above considerations into account, the system $[P_{66614}][FeCl_4]$ expectedly shows a lower value (255 kJ mol^{-1}) than the system $[P_{66614}]_3[GdCl_6]$ (604 kJ mol^{-1}).

3.2. Structural Properties

3.2.1. RDF analysis

Over the production runs, the RDFs using the GROMACS in-built tools were obtained. Figure 4 shows the RDFs for the centre of mass (COM) of the cation and anion of each targeted MIL system.

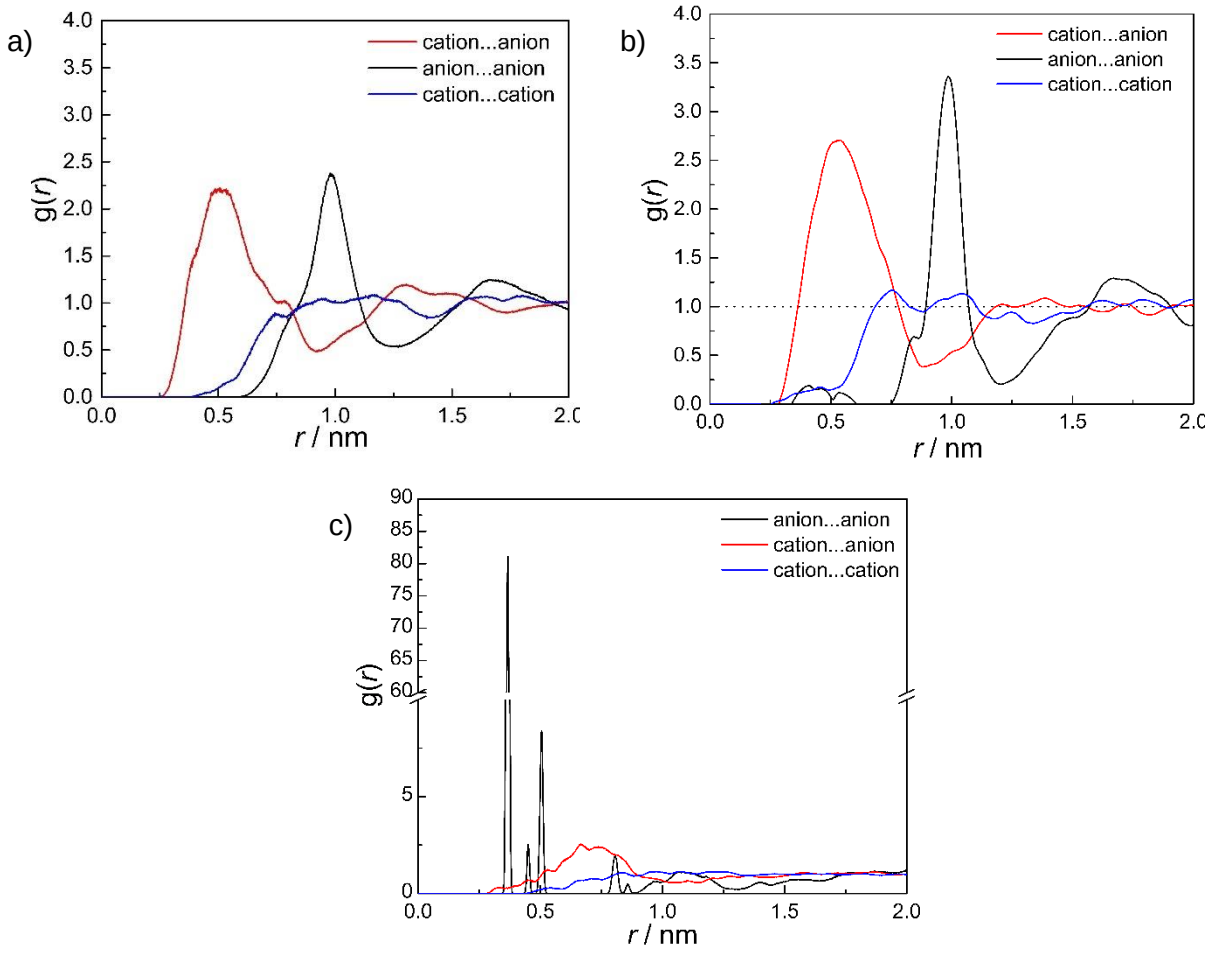

Figure 4. COM–COM radial distribution functions, $g(r)$, between cation and anion (red), cation and cation (blue) and anion and anion (black) in the MILs: a) $[P_{66614}][FeCl_4]$, b) $[P_{66614}]_2[MnCl_4]$, and c) $[P_{66614}]_3[GdCl_6]$, at 298.15 K.

As expected, the cation-anion interaction is represented by a better-defined first peak and at a closer distance than the others. For example, in the $[P_{66614}][FeCl_4]$ and

$[P_{66614}]_2[MnCl_4]$ systems, it is around 0.5 nm and, in the $[P_{66614}]_3[GdCl_{6,}]$ this peak is damped and appears at a longer distance, approximately at 0.75 nm. This value for the cation-anion distance can indicate that the anion is embedded in the alkyl chain of the cation [54].

The anion-anion interaction is slightly less significant as it appears at a greater distance (approximately 1 nm). Cation-cation interactions are practically negligible. This behaviour can be attributed to the length of the alkyl chain of the cation, where van der Waals forces predominate, and reflects the decrease in structural ordering at greater distances, characteristic of liquids (the peak is much lower and broader) [54].

It was also computed the atom-atom RDFs for the cation phosphorous atom (P3), cation C1P group – i.e.: carbon immediately after phosphorus, and the anion central atom, as shown in Figure 5 (see Figure 1 for atom notations).

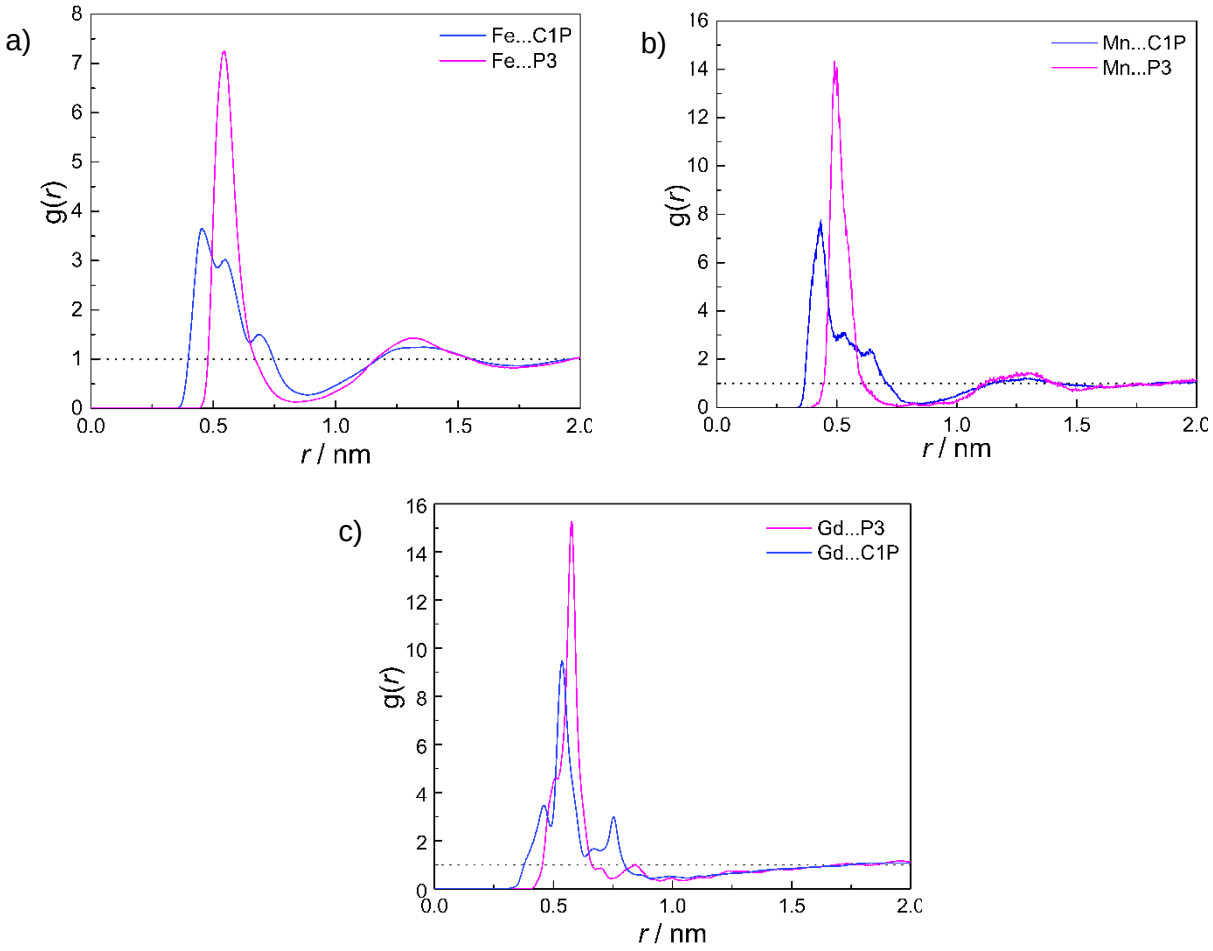

Figure 5. Radial distribution functions, $g(r)$, for anion central atom/P3 and anion central atom/C1P, for a) $[P_{66614}][FeCl_4]$, b) $[P_{66614}]_2[MnCl_4]$, and c) $[P_{66614}]_3[GdCl_6]$, at 298.15 K.

The analysis of these RDFs revealed that the metal atoms in the system have a pronounced affinity for the phosphorus atom and the carbons attached to it (C1P). This tendency is particularly pronounced in the MILs containing Mn and Gd (as evidenced by an intense peak). The affinity for the P3 atom can be explained by considering the charges, since the charge of the cation is localised at the phosphorous atom. The peak corresponding to the interaction of the iron metal with C1P appears at smaller distances, due to its proximity to P3, eventually "surrounding" the phosphorus atom, so that the different metal ions will primarily interact with these carbons. However, this peak is not high and defined enough, considering that Fe, Mn, and Gd show more affinity for the phosphorus atom.

3.2.2. SDF analysis

The Spatial Distribution Functions (SDFs) were also computed, allowing for a visual inspection of the probability of finding a particular observed site around a particular reference site.

Figure 6 shows the spatial arrangement of the iso-surfaces of the central atom of the anion around the reference molecule – i.e.: the P3 atom of the cation.

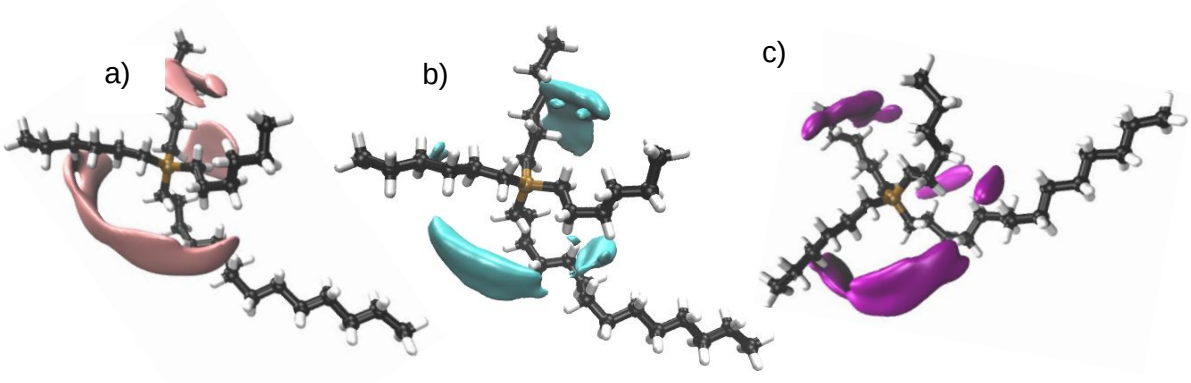

Figure 6. Spatial distribution functions (SDFs) for a) [P66614][$FeCl_4$], b) [P66614]$_2$[$MnCl_4$], and c) [P66614]$_3$[$GdCl_6$] systems, at 298 K. The black, white, brown, green, pink, cyan, and purple represent carbon, hydrogen, phosphorus, chloride, iron, manganese, and gadolinium atoms, respectively.

The effects that were discussed in the RDFs are clearly evident in the corresponding SDFs. The iso-surface of the anion is primarily situated in the areas surrounding the C1P atoms of the reference molecule. This is because the metallic ion of the anion is attracted to P3 due to the charges, as suggested by the RDF analysis.

3.3. Gas Adsorption by MILs

3.3.1. Solvation free energy

Our primary focus is on the adsorption of CO_2 in MILs, however $[P_{66614}][FeCl_4]$ was also explored for the possibility of other potentially dangerous gases capture. The effect of the temperature on the gas capture process was also addressed. Figure 7 is intended to demonstrate the different study perspectives that were applied.

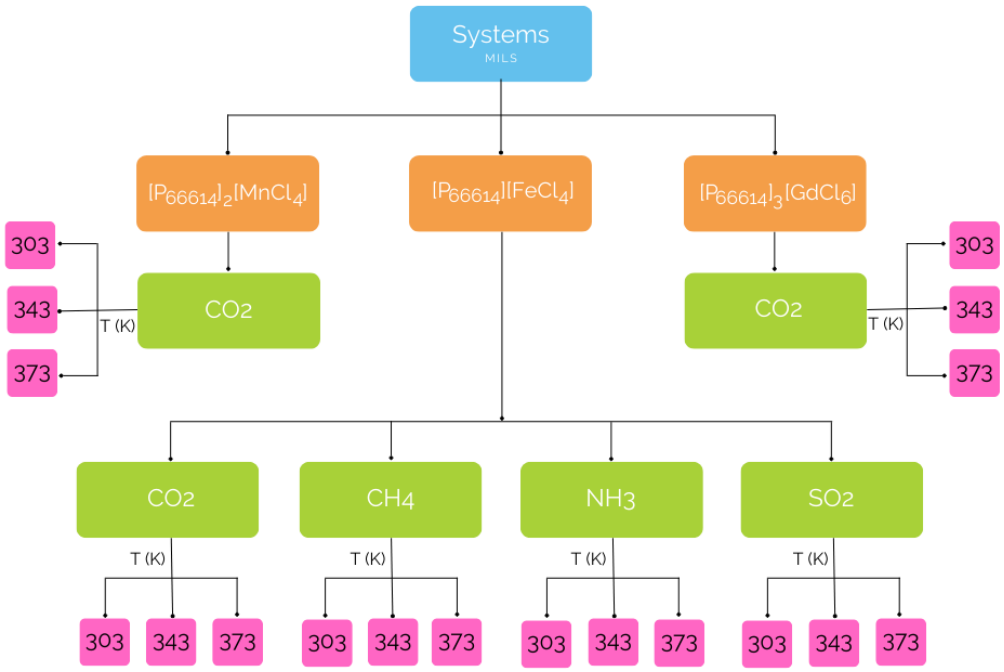

Figure 7. Study protocol employed.

The value of ΔG was obtained using Gromacs tools, after collecting all the md*.xvg files, for each λ value. This md files contain $\partial H/\partial\lambda$ data, which allows tracing a plot from which ΔG can be derived, where the free energy change from $\lambda = 0$ to $\lambda = 1$ is the sum of the free energy changes of each pair of neighbouring λ simulations, with the ΔG values corresponding to the first half of the results shown in the graphs obtained. The results for the different conditions and systems are presented in Table 6.

Table 6. Simulated free energy of solvation at different temperatures, with respective standard deviations.

MIL	Gases	Temperature	ΔG /kJ mol^{-1}	SD_{sim}
$[P_{66614}][FeCl_4]$	CH_4	303	1.5	0.2
		343	2.4	0.1
		373	2.6	0.1
	CO_2	303	0.3	0.1
		343	1.4	0.2
		373	1.9	0.2
	NH_3	303	3.9	0.2
		343	4.7	0.1
		373	5.2	0.1
	SO_2	303	-2.7	0.3
		343	-2.1	0.2
		373	-1.1	0.2
$[P_{66614}]_2[MnCl_4]$	CO_2	303	-1.7	0.3
		343	0.6	0.3
		373	1.3	0.3
$[P_{66614}]_3[GdCl_6]$	CO_2	303	-1.4	0.2
		343	-0.8	0.2
		373	-0.5	0.2

Looking at the values presented in Table 6, one can see that, in $[P_{66614}][FeCl_4]$, only the adsorption of SO_2 occurs spontaneously at all three addressed temperatures. The most promising results are obtained at 303 K, with a ΔG value of –2.66 kJ mol^{-1}. In contrast, for all other gases, the computed ΔG values are positive, indicating non-spontaneous adsorption. It is worth noting also that SO_2 benefits from favourable interactions with both the cation and anion, which likely contributes to its efficient capture. When comparing the adsorption of the different gases studied in these MILs, it is evident that gases containing hydrogen atoms exhibit less favourable ΔG values. Additionally, gases with lower densities are more challenging to capture. Two MILs, namely $[P_{66614}]_2[MnCl_4]$ and $[P_{66614}]_3[GdCl_6]$ show negative CO_2 adsorption energies, which makes them promising candidates for CO_2 removal.

The system with the anion $[GdCl_6]^{3-}$ showed better results than $[MnCl_4]^{2-}$, taking into account that in the latter the reaction does not occur spontaneously at 343 K nor at 373 K. This indicates that a higher number of unshared electron pairs enhances the effectiveness and promise of magnetic ionic liquids in CO_2 capture. For instance, when

comparing $[MnCl_4]^{2-}$ with two unshared electron pairs at 343 K (ΔG (CO_2) = +0.63 kJ mol^{-1}) to $[GdCl_6]^{3-}$ with three unshared electron pairs (ΔG (CO_2) = –0.80 kJ mol^{-1}). Thus, considering other studies with different ILs [12], our results confirm that highly electronegative anions will perform better. As expected, in all cases, lower temperatures favour the process.

3.3.2. Structural analysis of gas adsorption

To better understand the structure of the systems under study, a further structural analysis was carried out. Firstly, the COM–COM RDFs between different gases and MIL $[P_{66614}][FeCl_4]$ were analysed. These RDFs are shown in Figures 8-11.

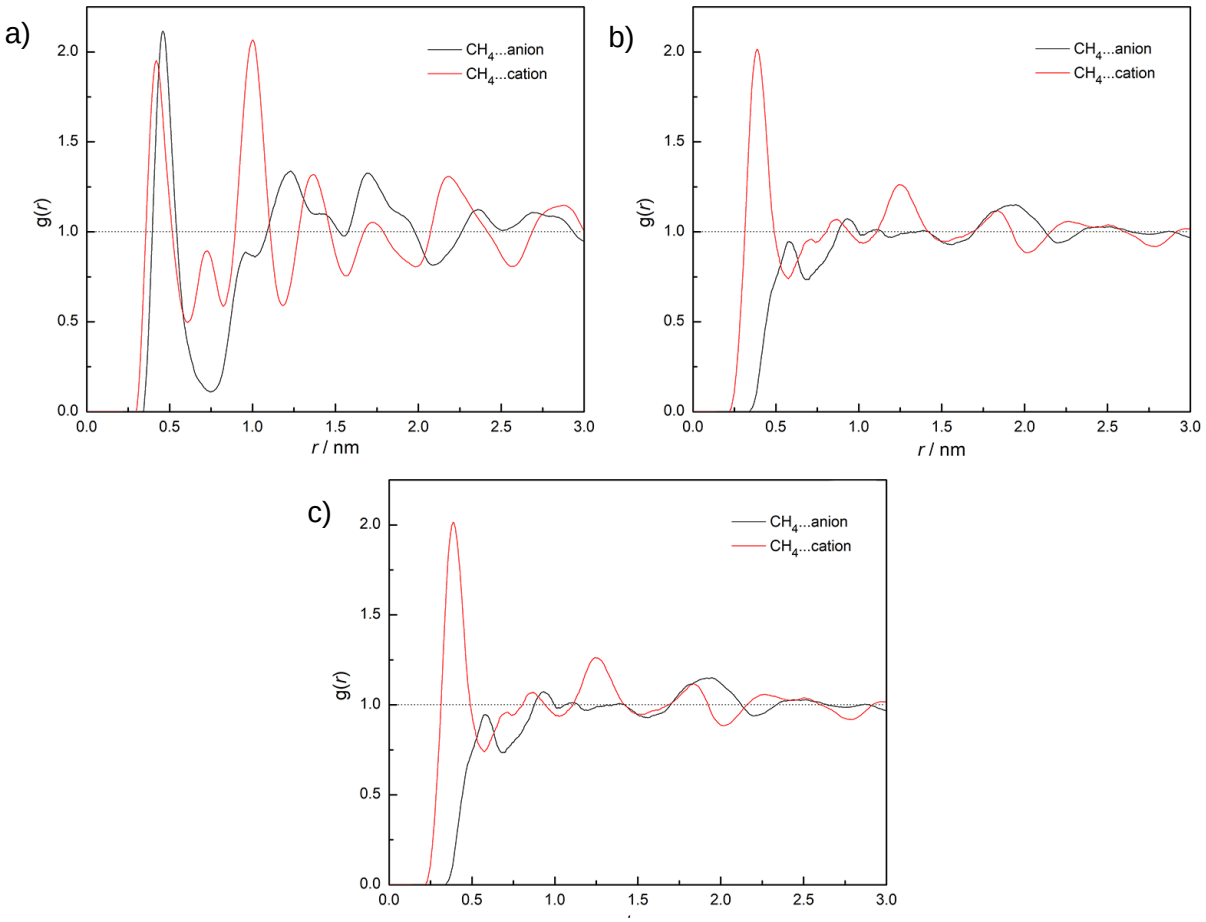

Figure 8. COM–COM radial distribution functions, $g(r)$, between CH_4 and anion (black) and CH_4 and cation (red) in $[P_{66614}][FeCl_4]$ at: a) 303.15 K, b) 343.15 K, and c) 373.15 K.

At lower temperatures, the interactions between CH_4 and both cation and anion of $[P_{66614}][FeCl_4]$ (see Figure 8) take place in a similar manner and at approximately the same distance, around 0.5 nm. With increasing temperature, the interactions between CH_4 and the cation become more predominant and shift to slightly shorter distances, around 0.4 nm, due to thermal motion. However, it is important to note that the CH_4–cation peak remains unchanged as the temperature rises, indicating no improvement in the interaction. This observation is in accordance with the ΔG values from Table 6.

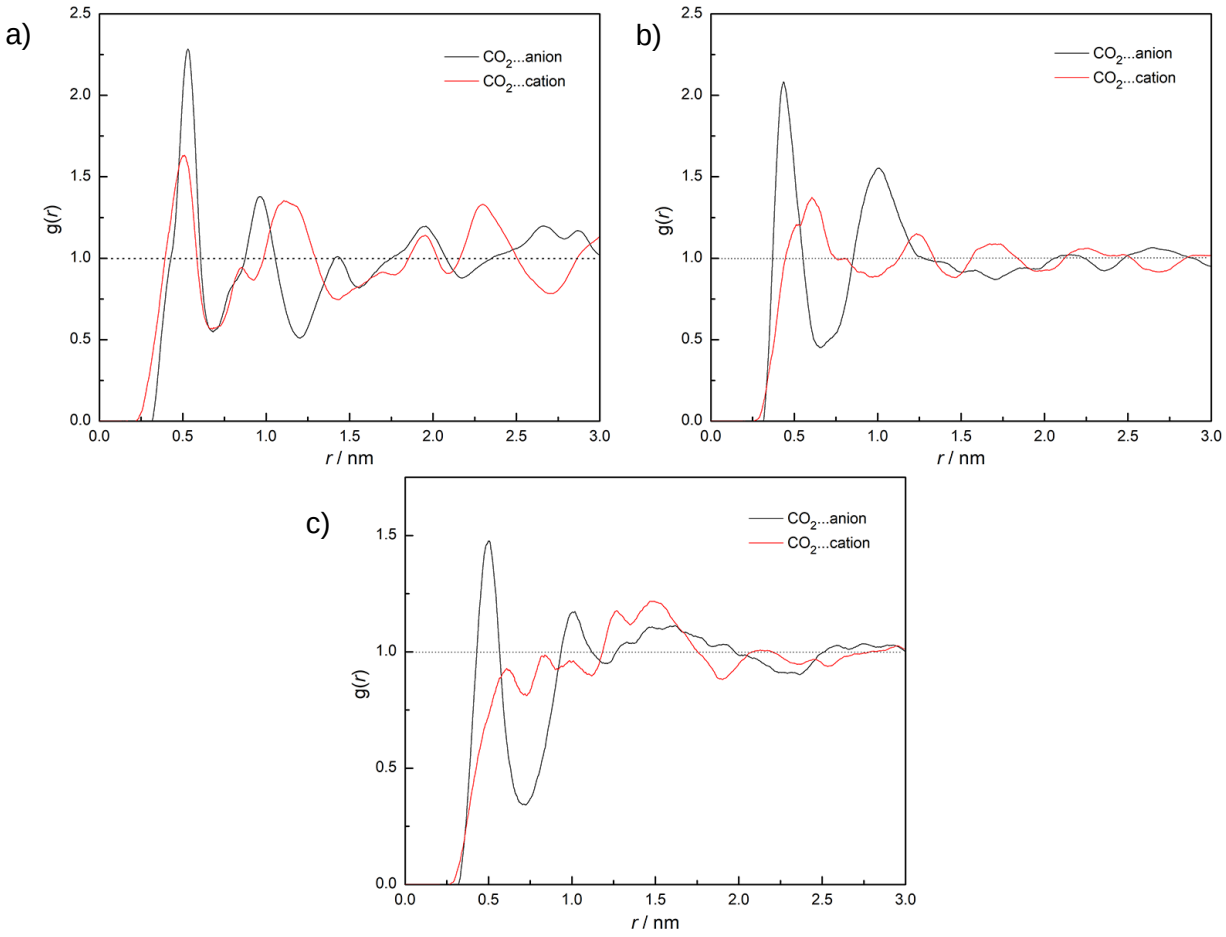

Figure 9. COM–COM radial distribution functions, $g(r)$, between CO_2 and anion (black) and CO_2 and cation (red) in $[P_{66614}][FeCl_4]$ at: a) 303.15 K, b) 343.15 K, and c) 373.15 K.

As for CO_2 gas (see Figure 9), the interaction with the ions expectedly appears at similar distance (~0.5 nm), presenting a higher and more well-defined first peak for the anion than for the cation. In addition, as the temperature rises, the peak for CO_2–anion interaction starts to lower, showing a decrease in the interaction, while the CO_2–cation

interaction becomes negligible. This aligns with the values presented in Table 6, where the ΔG values increase with increasing temperature, indicating a less unfavourable reaction.

Regarding interactions with NH_3, the behaviour exhibits similarities with both previously discussed cases: similar to CO_2, the interaction of gas NH_3 with the anion predominates, especially at higher temperatures; similar to CH_4, the interaction with the cation diminishes and shifts from an initial distance of approximately 0.5 nm (at 298.15 K) to about 0.4 nm (at 373.15 K). Interestingly, at lower temperatures, the shortest distance is observed for the NH_3–anion interaction, whereas at higher temperatures, the NH_3–cation interaction becomes the closest.

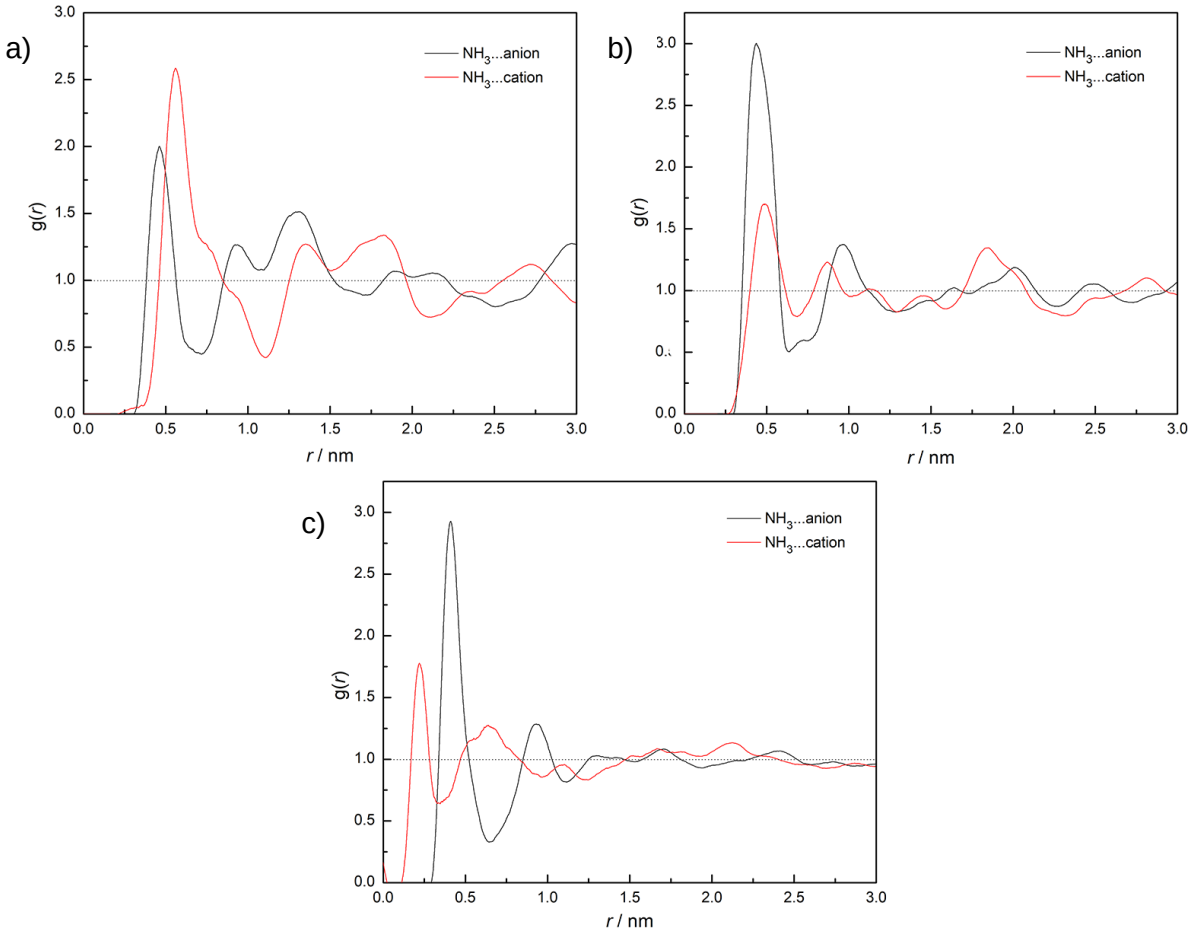

Figure 10. COM–COM radial distribution functions, $g(r)$, between NH_3 and anion (black) and NH_3 and cation (red) in $[P_{66614}][FeCl_4]$ at: a) 303.15 K, b) 343.15 K, and c) 373.15 K.

Since SO_2 is the only gas that has shown promise for being captured at lower temperatures, the analysis of the corresponding RDFs may be more insightful. As we can see from the RDFs obtained for this gas (see Figure 11), the SO_2–anion and SO_2–cation first interaction peaks are located at approximately the same distance, with both being well defined, thus showing the participation of both the anion and the cation in the capture of this gas.

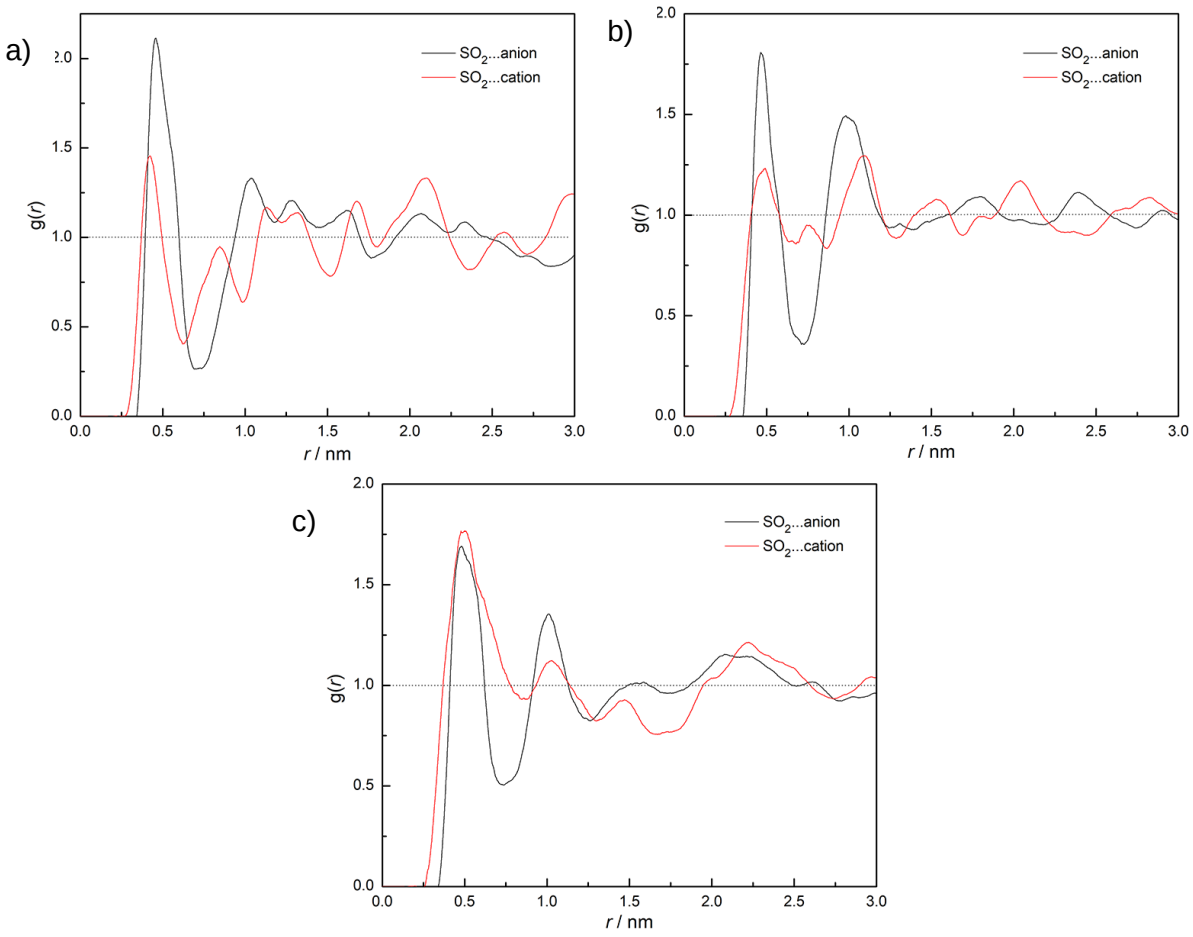

Figure 11. COM–COM radial distribution functions, $g(r)$, between SO_2 and anion (black) and SO_2 and cation (red) in [P66614][$FeCl_4$] at a) 303.15 K, b) 343.15 K, and c) 373.15 K.

To continue with the analysis of local structure in the studied systems, the atom–atom RDFs were assessed. Given the fact, that in most of the cases, the interaction between gas and anion predominates, only the chlorine atom and the central atom of each anion were considered for analysing interactions with the gas molecule. Atom–atom RDFs for the gas–cation are not presented (see Figures 12-15), as the COM–COM RDFs showed that these interactions are practically negligible. However, an example of gas interaction with the central atom of the cation, P3, can be seen in the Appendix 2.

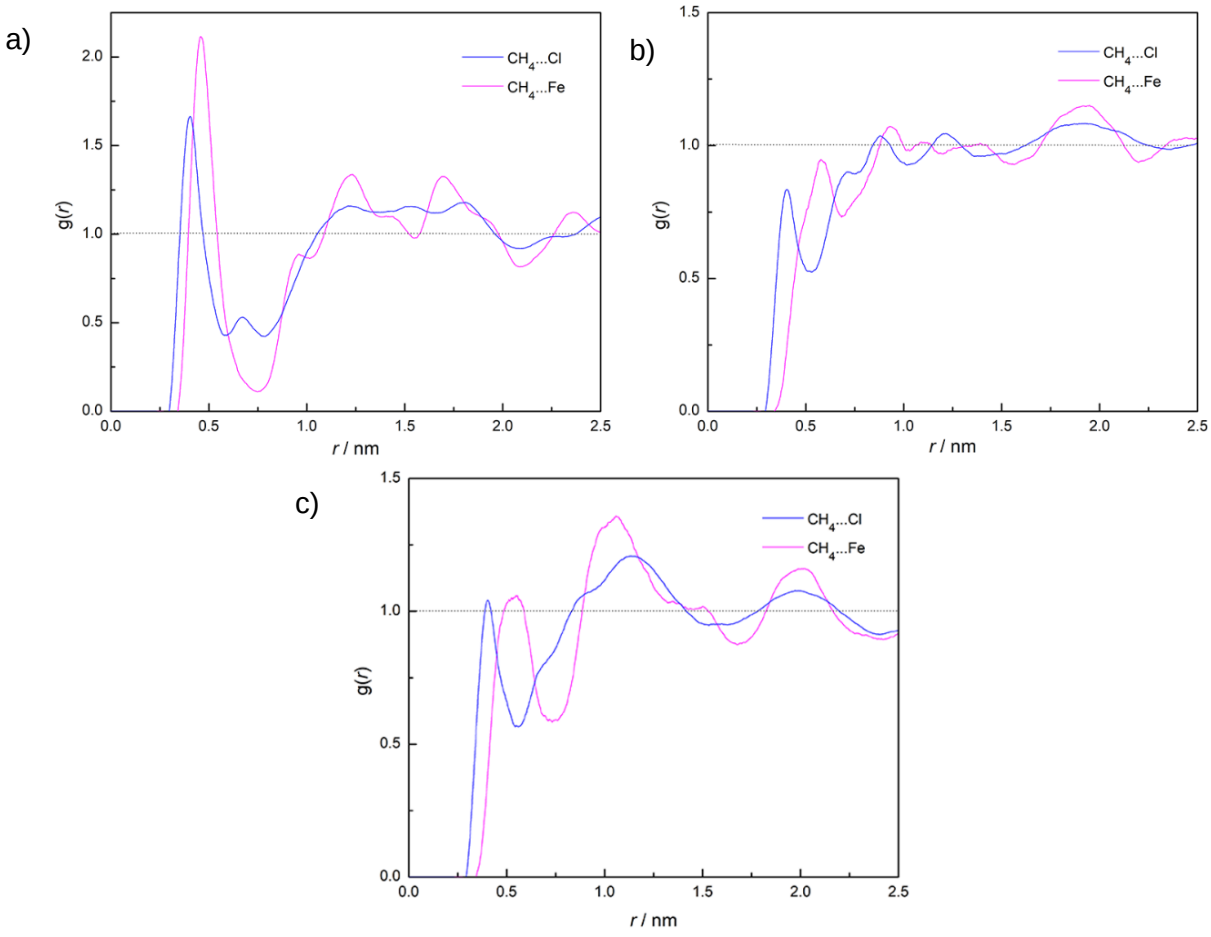

Figure 12. Radial distribution functions, $g(r)$, for CH_4 gas/Cl (blue) and CH_4 gas/Fe (pink), for $[P_{66614}][FeCl_4]$ at a) 303.15 K, b) 343.15 K, and c) 373.15 K.

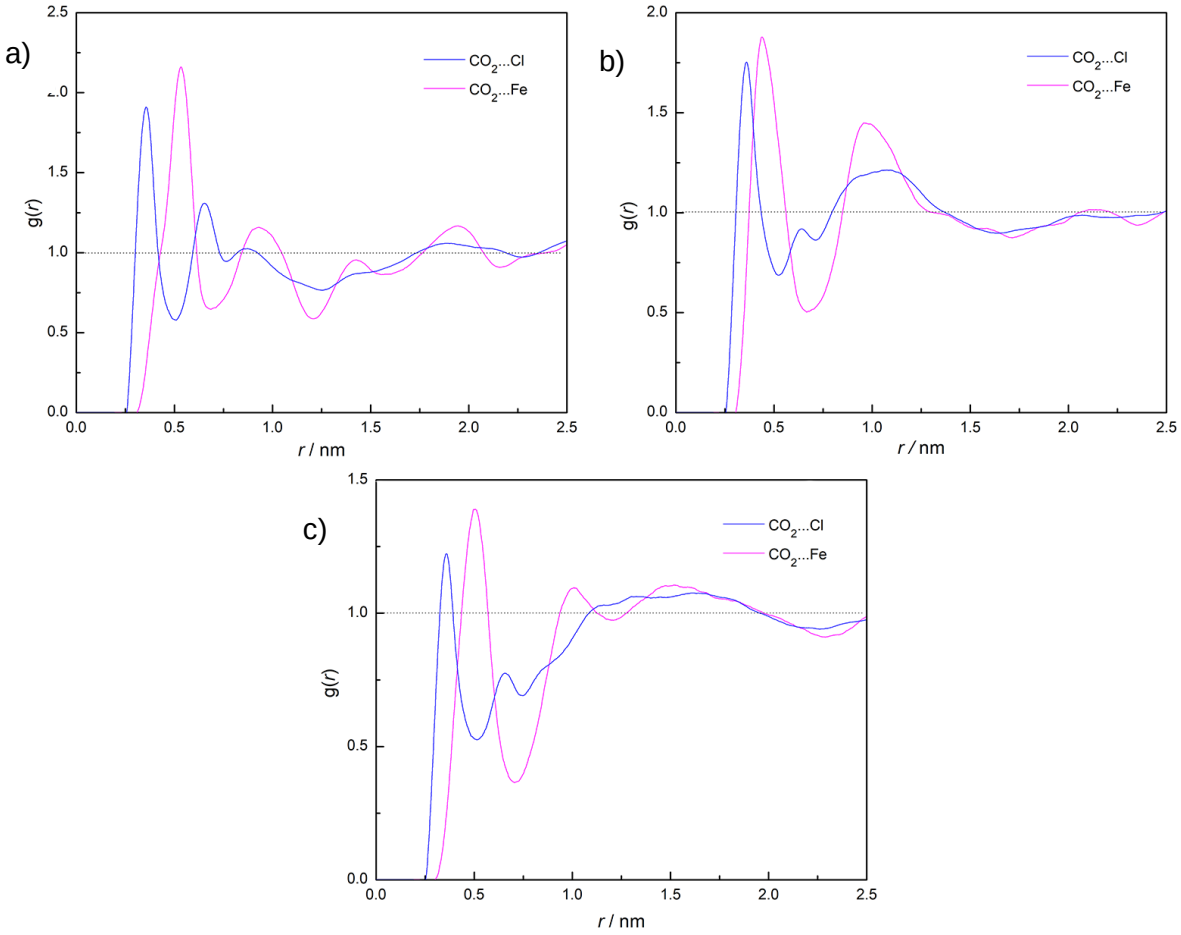

Figure 13. Radial distribution functions, $g(r)$, for CO_2 gas/Cl (blue) and CO_2 gas/Fe (pink), for $[P_{66614}][FeCl_4]$ at a) 303.15 K, b) 343.15 K, and c) 373.15 K.

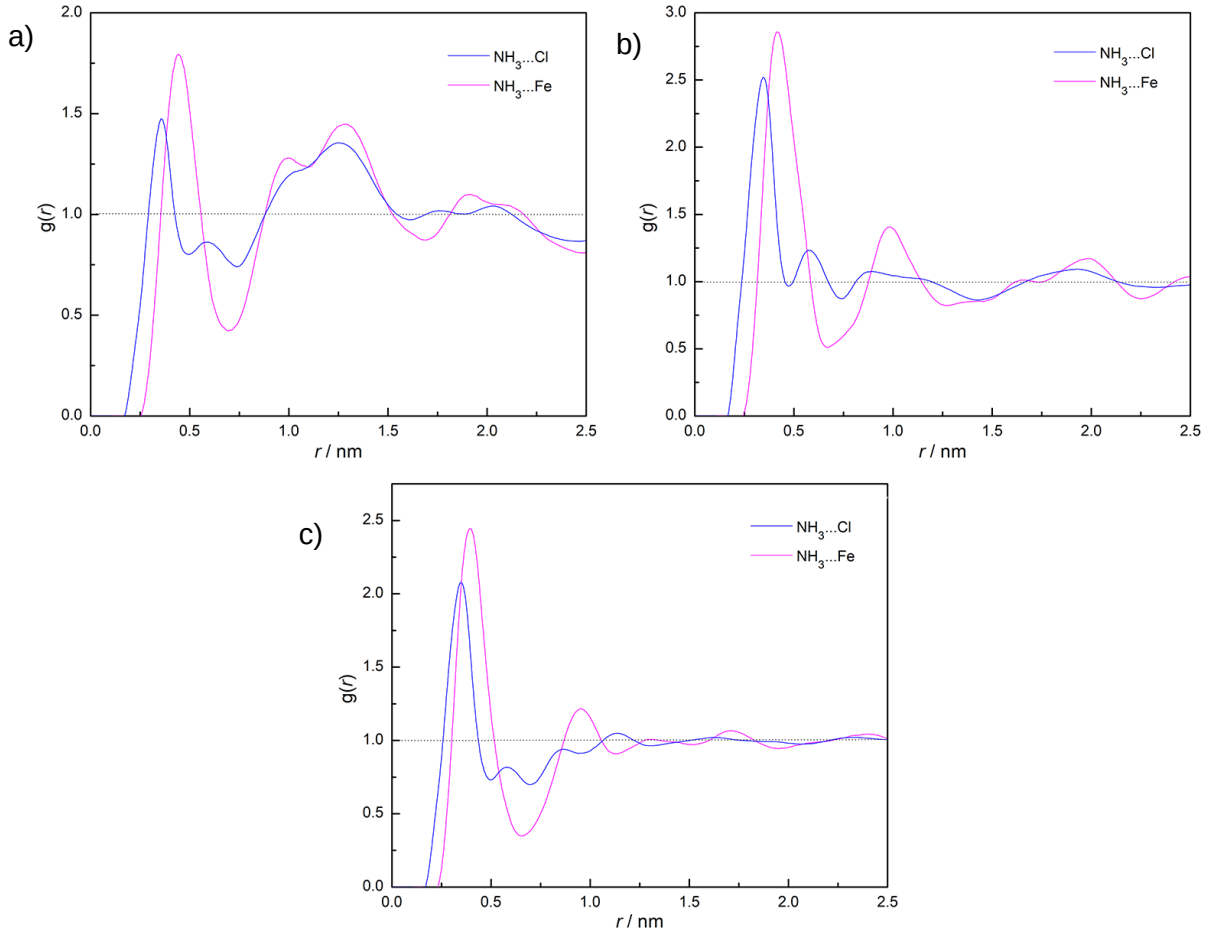

Figure 14. Radial distribution functions, *g*(*r*), for NH_3 gas/Cl (blue) and NH_3 gas/Fe (pink), for $[P_{66614}][FeCl_4]$ at a) 303.15 K, b) 343.15 K, and c) 373.15 K.

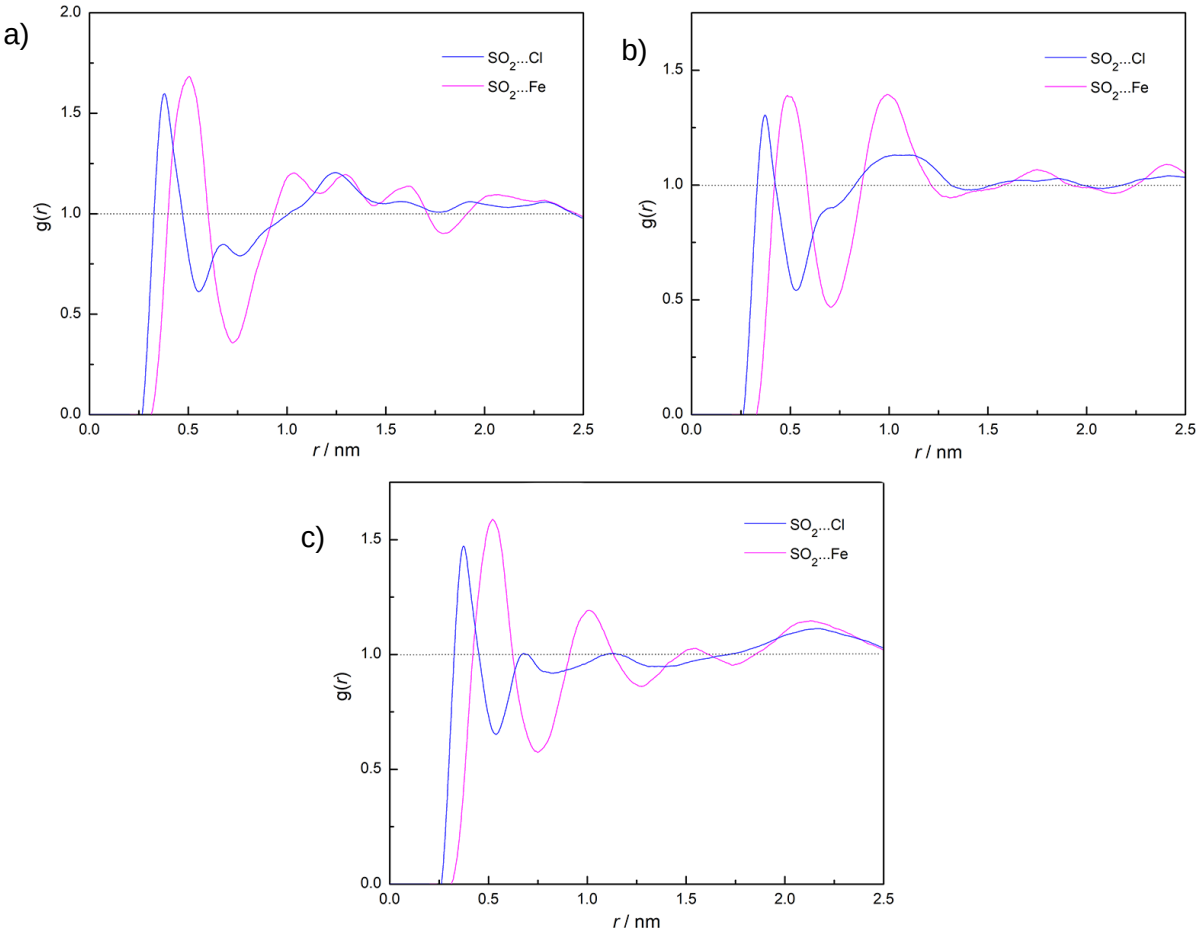

Figure 14. Radial distribution functions, $g(r)$, for SO_2 gas/Cl (blue) and SO_2 gas/Fe (pink), for $[P_{66614}][FeCl_4]$ at a) 303.15 K, b) 343.15 K, and c) 373.15 K.

As expected, all gases interact with both atoms of the anion, with the Cl atom at shorter distances and with Fe at longer, due to geometry of anion. CH_4 gas presents somewhat a different interaction pattern: meaningful interactions can only be seen at 298.15 K, which is in agreement with COM–COM RDFs shown in Figure 8.

A similar study was then carried out for the remaining MILs to infer about the impact of other anions on CO_2 capture. Figures 16 and 17 display COM–COM RDFs at various temperatures for the systems $[P_{66614}]_2[MnCl_4]$ and $[P_{66614}]_3[GdCl_6]$, respectively.

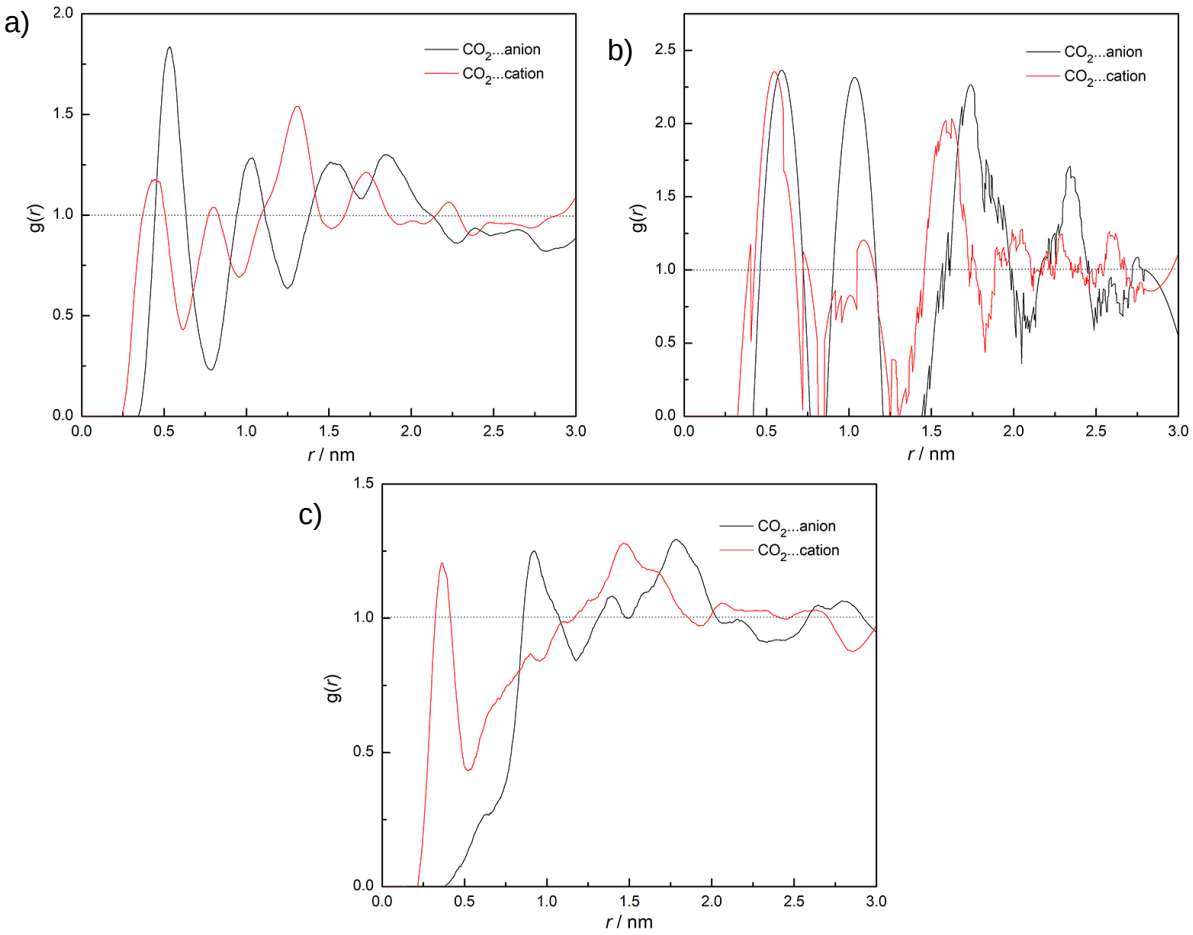

Figure 15. COM–COM radial distribution functions, $g(r)$, between CO_2 and anion (black) and CO_2 and cation (red) in $[P_{66614}]_2[MnCl_4]$ at: a) 303.15 K, b) 343.15 K, and c) 373.15 K.

As expected, CO_2 shows a first peak corresponding to a strong interaction with the anion $[MnCl_4]^{2-}$ (Figure 16) at low temperatures, where the ΔG calculation showed promise in capturing CO_2 gas. However, at the highest temperature, an inversion occurs, and the CO_2–cation first peak becomes more pronounced. At the intermediate temperature, both cation–CO_2 and anion–CO_2 interaction peaks coincide.

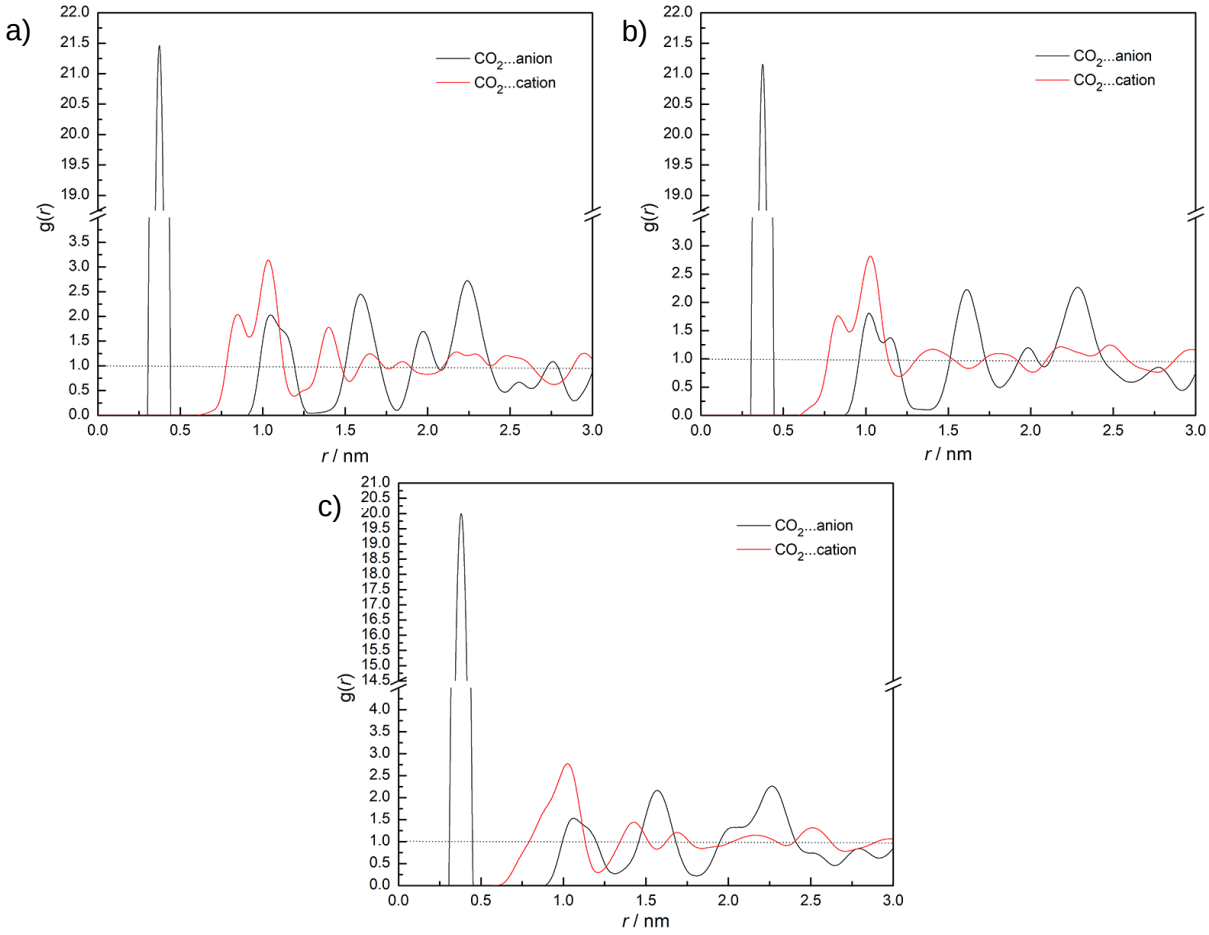

Figure 16. COM–COM radial distribution functions, $g(r)$, between CO_2 and anion (black) and CO_2 and cation (red) in $[P_{66614}]_3[GdCl_6]$ at: a) 303.15 K, b) 343.15, K, and c) 373.15 K.

In the case of $[P_{66614}]_3[GdCl_6]$ MIL (Figure 17), independently of the temperature, the peaks of interaction with the anion are the most defined and the highest. These appear at a notably smaller distance, compared to the other systems. This is in agreement with the ΔG values reported in Table 6, where MIL $[P_{66614}]_3[GdCl_6]$ was shown to be the most promising for CO_2 gas capture. This is an expected behaviour, taking into account the number of unshared electrons of the anion.

The atom–atom RDFs of the different systems were also compared in order to understand the impact of the central atom of the anion on CO_2 capture. This type of RDFs for the MILs $[P_{66614}]_2[MnCl_4]$ and $[P_{66614}]_3[GdCl_6]$ are depicted in Figures 18 and 19, respectively.

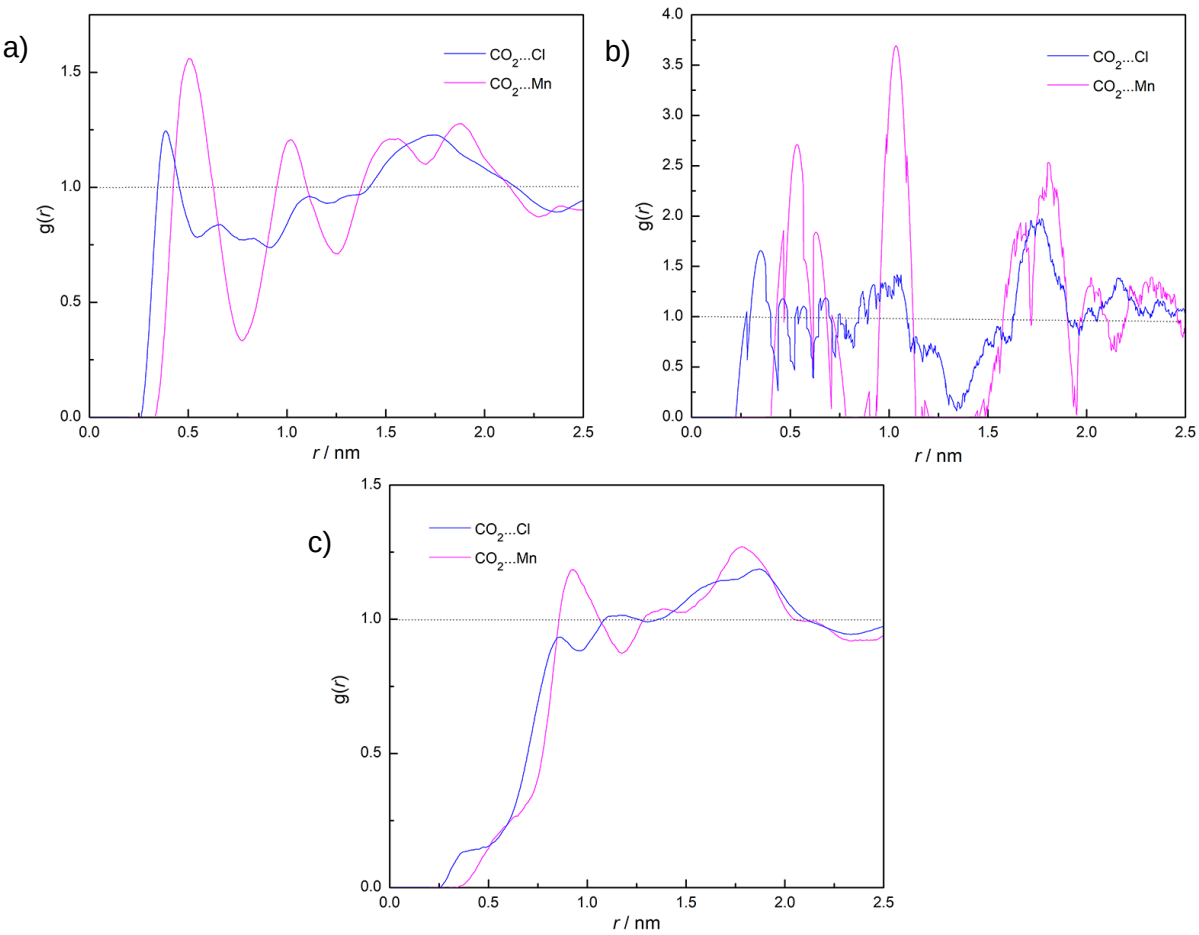

Figure 17. Radial distribution functions, *g*(r), for CO_2 gas/Cl (blue) and CO_2 gas/Fe (pink), for $[P_{66614}]_2[MnCl_4]$ at a) 303.15 K, b) 343.15 K, and c) 373.15 K.

By comparing the atom–atom RDF in MIL $[P_{66614}][FeCl_4]$ (Figure 13) with the ones of these two systems (Figures 18 and 19), we can see that the interactions take place at a shorter distance (0.3-0.4 nm), which may show their ability to capture the CO_2 gas. At the same time, in $[P_{66614}]_2[MnCl_4]$ MIL at 373.15 K (see Figure 18), the interactions with CO_2 are negligible, showing no hope for high-temperature CO_2 capture.

Moreover, these atomic distances are even shorter for the $[P_{66614}]_3[GdCl_6]$ system, as can be seen in Figure 19.

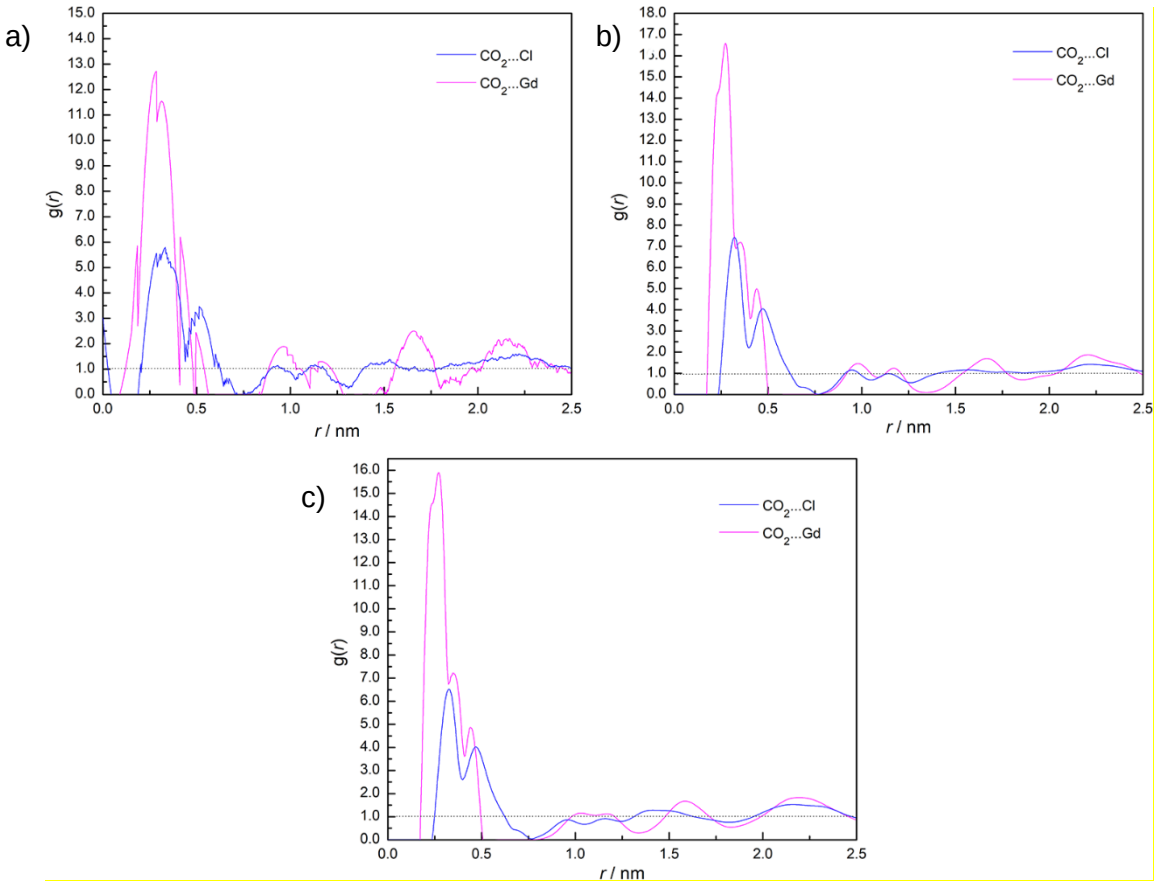

Figure 18. Radial distribution functions, $g(r)$, for CO_2 gas/Cl (blue) and CO_2 gas/Fe (pink), for $[P_{66614}]_3[GdCl_6]$ at a) 303.15 K, b) 343.15 K, and c) 373.15 K.

To sum up, the analysis of the different atom–atom RDFs reveals that as the number of unshared electrons increases, the distance between the central atom of the anion and CO_2 becomes shorter and more defined. The peak of the interaction with Cl is now observed at a greater distance than the peak of the interaction with the central atom. This indicates an increased ease of interaction or approach to the central atom, which aligns with the conclusions drawn from the ΔG values. Indeed, as follows from the analysis of the ΔG values in Table 6, more promising results for gas capture are achieved for MILs containing an anion with greater number of unshared electrons.

4. Conclusions

In this work, we carried out molecular dynamics simulation of three MILs, namely: phosphonium tretrachloroferrate ($[P_{66614}][FeCl_4]$), phosphonium tretrachloromanganese ($[P_{66614}]_2[MnCl_4]$), and phosphonium hexachlorogadolinium, ($[P_{66614}]_3[GdCl_6]$), with the aim of assessing their potential for capturing greenhouse and potentially hazardous gases, such as CO_2, SO_2, NH_3, or CH_4. Initially, we validated the FFs previously developed in our group for these MILs. Given the complexity and high viscosity of phosphonium-based MILs, atomistic studies of these materials are relatively rare. Therefore, we explored various simulation methods to investigate transport properties (such as viscosity using non-equilibrium MD, Green-Kubo, and the Einstein relation; self-diffusion using mean square displacement and velocity autocorrelation functions), as well as calculated the density and enthalpy of vaporisation. Additionally, we performed a structural analysis in terms of radial and spatial distribution functions. Our analysis of viscosity using the Einstein's Relation revealed that, generally, with increasing temperature (resulting in less viscous MILs), the values closely align with experimental data. For self-diffusion, the method based on MSD appears to produce more accurate results. Therefore, our FFs effectively reproduce experimental data and can be confidently applied to future gas capture studies.

Following FF validation, we proceeded to evaluate the capacity of these three MILs to capture greenhouse gases, with a primary focus on CO_2 adsorption. Additionally, we explored $[P_{66614}][FeCl_4]$ for its potential to capture other potentially dangerous gases. Our findings were rationalised in terms of solvation free energy and radial distribution functions.

Notably, only SO_2 adsorption appears to occur spontaneously in $[P_{66614}][FeCl_4]$, while for all other gases, the ΔG values were positive. Two other MILs have negative CO_2 adsorption energies, making them promising candidates for CO_2 capture. Temperature was also found to have the expected effect on the gas capture process, with lower temperatures promoting the process. In terms of local structures, as revealed by RDF analysis, all gases, except for CH_4, expectedly exhibited stronger interactions with the anion than with the cation. Also, as evidenced by comparison of ΔG values and local structure in the systems with CO_2, the higher content of unshared electron pares in anion, the more promising is the MIL for gas capture.

5. References

[1] N. O. Feider, S. M. Mahurin, C.-L. Do-Thanh, S. Dai, D.-e. Jiang, *Journal of Molecular Liquids* **2021**, *335*, 116163.
[2] S. K. Singh, A. W. Savoy, *Journal of Molecular Liquids* **2020**, *297*, 112038.
[3] Z. Lei, C. Dai, B. Chen, *Chemical reviews* **2014**, *114*, 1289-1326.
[4] E. Santos, J. Albo, A. Rosatella, C. A. Afonso, A. Irabien, *Journal of Chemical Technology & Biotechnology* **2014**, *89*, 866-871.
[5] Eurosat, Statistics explained, **2022**. Retrieved from https://ec.europa.eu/eurostat/statistics-explained/, acessed on june 2023
[6] G. J. MacDonald, *Annual review of energy* **1990**, *15*, 53-83.
[7] N. Bragagnolo, C. A. Silva, M. H. Taniwaki, *Revista do Instituto Adolfo Lutz* **2001**, *60*, 103-107.
[8] S. A. Pierson, O. Nacham, K. D. Clark, H. Nan, Y. Mudryk, J. L. Anderson, *New Journal of Chemistry* **2017**, *41*, 5498-5505.
[9] E. Santos, J. Albo, A. Irabien, *Rsc Advances* **2014**, *4*, 40008-40018.
[10] W. Chen, S. Liang, Y. Guo, X. Gui, D. Tang, *Fluid Phase Equilibria* **2013**, *360*, 1-6.
[11] E. J. Maginn, R. A. Messerly, D. J. Carlson, D. R. Roe, J. R. Elliot, *Living Journal of Computational Molecular Science* **2019**, *1*, 6324-6324.
[12] N. Islam, H. Warsi Khan, A. A. Gari, M. Yusuf, K. Irshad, *Fuel* **2022**, *330*, 125540.
[13] P. Walden, *Известия Российской академии наук. Серия математическая* **1914**, *8*, 405-422.
[14] J. F. Brennecke, E. J. Maginn, *American Institute of Chemical Engineers. AIChE Journal* **2001**, *47*, 2384.
[15] J. P. Hallett, T. Welton, *Chemical reviews* **2011**, *111*, 3508-3576.
[16] K. R. Seddon, A. Stark, M.-J. Torres, *Pure and Applied Chemistry* **2000**, *72*, 2275-2287.
[17] R. D. Rogers, K. R. Seddon, *Ionic liquids IIIB: fundamentals, progress, challenges, and opportunities: transformations and processes, Vol. 902*, American Chemical Society, **2005**.
[18] N. D. Khupse, A. Kumar, *Indian Journal Of Chemistry* **2010**, *Vol.49A*, 635-648.
[19] K. D. Clark, O. Nacham, J. A. Purslow, S. A. Pierson, J. L. Anderson, *Analytica chimica acta* **2016**, *934*, 9-21.
[20] M. Sajid, *TrAC Trends in Analytical Chemistry* **2019**, *113*, 210-223.
[21] S. Hayashi, H.-o. Hamaguchi, *Chemistry Letters* **2004**, *33*, 1590-1591.
[22] R. E. Del Sesto, T. M. McCleskey, A. K. Burrell, G. A. Baker, J. D. Thompson, B. L. Scott, J. S. Wilkes, P. Williams, *Chemical Communications* **2008**, 447-449.
[23] P. Nockemann, B. Thijs, N. Postelmans, K. Van Hecke, L. Van Meervelt, K. Binnemans, *Journal of the American Chemical Society* **2006**, *128*, 13658-13659.
[24] B. Mallick, B. Balke, C. Felser, A. V. Mudring, *Angewandte Chemie International Edition* **2008**, *47*, 7635-7638.
[25] J. Albo, E. Santos, L. Neves, S. Simeonov, C. Afonso, J. Crespo, A. Irabien, *Separation and purification technology* **2012**, *97*, 26-33.
[26] Y. Yoshida, G. Saito, in *Ionic Liquids: theory, properties, new approaches* (Ed.: P. A. Kokorin), InTech, **2011**.
[27] R. C. Reid, J. M. Prausnitz, B. E. Poling, *The properties of gases and liquids*, 5th ed., New York: McGraw-Hill Education, **1987**.

[28] C. Daniel, J. Albo, E. Santos, C. Portugal, J. Crespo, A. Irabien, *Fluid Phase Equilibria* **2013**, *360*, 29-35.
[29] B. J. Alder, T. E. Wainwright, *The Journal of Chemical Physics* **1960**, *33*, 1439-1451.
[30] K. Binder, J. Horbach, W. Kob, W. Paul, F. Varnik, *Journal of Physics: Condensed Matter* **2004**, *16*, S429.
[31] A. Hospital, J. R. Goñi, M. Orozco, J. L. Gelpí, *Advances and Applications in Bioinformatics and Chemistry* **2015**, *8*, 37-47.
[32] F. Fernandes, *Química, Boletim da Sociedade Portuguesa de Química* **2003**, *90*, 39-43.
[33] W. L. Jorgensen, J. Tirado-Rives, *Journal of the American Chemical Society* **1988**, *110*, 1657-1666.
[34] J. N. Canongia Lopes, J. Deschamps, A. A. H. Pádua, *The Journal of Physical Chemistry B* **2004**, *108*, 2038-2047.
[35] M. R. Shirts, J. W. Pitera, W. C. Swope, V. S. Pande, *The Journal of Chemical Physics* **2003**, *119*, 5740-5761.
[36] N.-T. Van-Oanh, C. Houriez, B. Rousseau, *Physical Chemistry Chemical Physics* **2010**, *12*, 930-936.
[37] B. Hess, *The Journal of chemical physics* **2002**, *116*, 209-217.
[38] T. Köddermann, D. Paschek, R. Ludwig, *ChemPhysChem* **2007**, *8*, 2464-2470.
[39] M. Kowsari, S. Alavi, M. Ashrafizaadeh, B. Najafi, *The Journal of chemical physics* **2008**, *129*, 224508.
[40] K. R. Harris, *The Journal of Chemical Physics* **2009**, *131*.
[41] R. R. Ratnakar, B. Dindoruk, *Processes* **2022**, *10*, 1194.
[42] E. S. C. Ferreira, I. V. Voroshylova, N. M. Figueiredo, C. M. Pereira, M. N. D. S. Cordeiro, *Journal of Molecular Liquids* **2020**, *298*, 111978.
[43] X. Wu, W. Sha, *Applied Surface Science* **2008**, *255*, 2813-2821.
[44] G. Harding, A. Harding, in *Counterterrorist detection techniques of explosives, Vol. Chapter 8* (Ed.: J. Yinon), Elsevier, **2007**, pp. 199-235.
[45] M. Brehm, B. Kirchner, *Journal of Chemical Information and Modeling* **2011**, *51*, 2007-2023.
[46] K. Kulińska, T. Kuliński, A. Lyubartsev, A. Laaksonen, R. W. Adamiak, *Computers & Chemistry* **2000**, *24*, 451-457.
[47] S. Jalili, M. Akhavan, *Journal of computational chemistry* **2010**, *31*, 286-294.
[48] E. P. Raman, T. J. Paul, R. L. Hayes, C. L. Brooks III, *Journal of chemical theory and computation* **2020**, *16*, 7895-7914.
[49] C. D. Christ, A. E. Mark, W. F. Van Gunsteren, *Journal of computational chemistry* **2010**, *31*, 1569-1582.
[50] A. Pohorille, C. Jarzynski, C. Chipot, *The Journal of Physical Chemistry B* **2010**, *114*, 10235-10253.
[51] C. S. M. Kang, X. Zhang, D. R. MacFarlane, *The Journal of Physical Chemistry C* **2018**, *122*, 24550-24558.
[52] Q. Parker, R. G. Bell, N. H. de Leeuw, *Molecular Simulation* **2021**, *47*, 152-160.
[53] R. Ge, C. Hardacre, J. Jacquemin, P. Nancarrow, D. W. Rooney, *Journal of Chemical & Engineering Data* **2008**, *53*, 2148-2153.
[54] A. Li, Z. Tian, T. Yan, D.-e. Jiang, S. Dai, *The Journal of Physical Chemistry B* **2014**, *118*, 14880-14887.

Appendices

Appendix 1 . Script to calculate the free energy of solvation.

```
#!/bin/bash

# Set some environment variables
FREE_ENERGY=`pwd`
echo "Free energy home directory set to $FREE_ENERGY"
MDP=$FREE_ENERGY/MDP
echo ".mdp files are stored in $MDP"

# Change to the location of your GROMACS-2018 installation
#GMX=/usr/local/gromacs/bin

for (( i=0; i<21; i++ ))
do
    LAMBDA=$i

    # A new directory will be created for each value of lambda and
    # at each step in the workflow for maximum organisation.

    mkdir Lambda_$LAMBDA
    cd Lambda_$LAMBDA

    ##############################
    # ENERGY MINIMIZATION STEEP  #
    ##############################
    echo "Starting minimization for lambda = $LAMBDA..."

    mkdir EM
    cd EM

    # Iterative calls to grompp and mdrun to run the simulations

      gmx_mpi grompp -f $MDP/em_steep_$LAMBDA.mdp -c
$FREE_ENERGY/NPT_preeq_2.gro -p $FREE_ENERGY/topol.top -o min$LAMBDA.tpr


      gmx_mpi mdrun -deffnm min$LAMBDA


  sleep 10
```

```
    ######################
    # NVT EQUILIBRATION #
    ######################
    echo "Starting constant volume equilibration..."

    cd ../
    mkdir NVT
    cd NVT

      gmx_mpi grompp -f $MDP/nvt_$LAMBDA.mdp -c ../EM/min$LAMBDA.gro -p
$FREE_ENERGY/topol.top -o nvt$LAMBDA.tpr

      gmx_mpi mdrun -deffnm nvt$LAMBDA

    echo "Constant volume equilibration complete."

    sleep 10

    ######################
    # NPT EQUILIBRATION #
    ######################
    echo "Starting constant pressure equilibration..."

    cd ../
    mkdir NPT
    cd NPT

      gmx_mpi grompp -f $MDP/npt_$LAMBDA.mdp -c ../NVT/nvt$LAMBDA.gro -p
$FREE_ENERGY/topol.top -t ../NVT/nvt$LAMBDA.cpt -o npt$LAMBDA.tpr


      gmx_mpi mdrun -deffnm npt$LAMBDA


    echo "Constant pressure equilibration complete."

   sleep 10
```

```
#################
    # PRODUCTION MD #
    #################
    echo "Starting production MD simulation..."

    cd ../
    mkdir Production_MD
    cd Production_MD

      gmx_mpi  grompp  -f  $MDP/md_$LAMBDA.mdp  -c  ../NPT/npt$LAMBDA.gro  -p
$FREE_ENERGY/topol.top -t ../NPT/npt$LAMBDA.cpt -o md$LAMBDA.tpr

      gmx_mpi mdrun -deffnm md$LAMBDA

    echo "Production MD complete."

    # End
    echo "Ending. Job completed for lambda = $LAMBDA"

    cd $FREE_ENERGY
done

exit;
```

Appendix 2

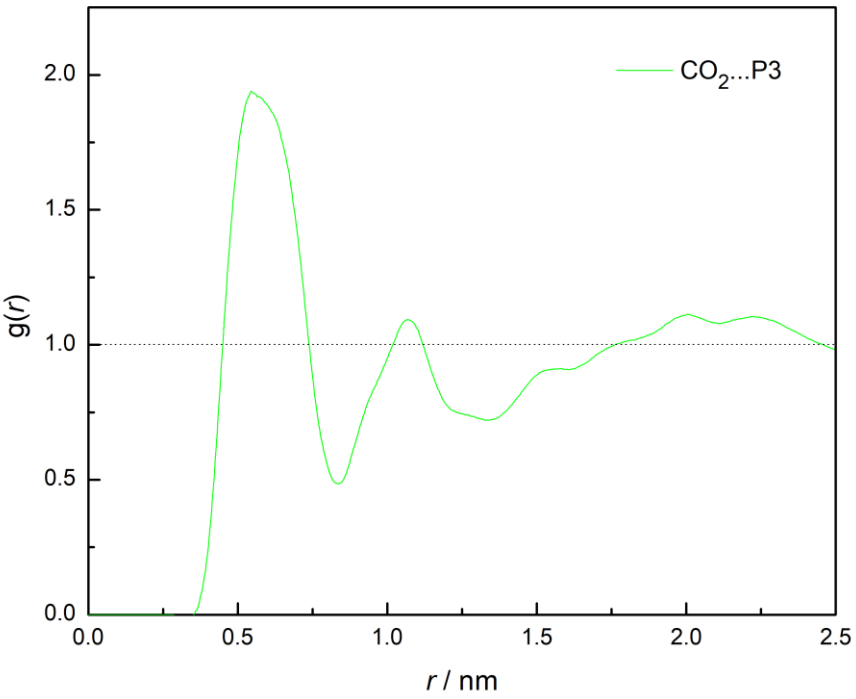

Figure A2.1. Radial distribution functions, $g(r)$, of CO_2 gas/P3 (green) for $[P_{66614}][FeCl_4]$ at 303.15 K.